Diverse Synoptic Weather Patterns of Warm-Season Heavy Rainfall Events in South Korea

CHANIL PARK,[a] SEOK-WOO SON,[a] JOOWAN KIM,[b] EUN-CHUL CHANG,[b] JUNG-HOON KIM,[a] ENOCH JO,[c]
DONG-HYUN CHA,[d] AND SUJONG JEONG[e]

[a] *School of Earth and Environmental Sciences, Seoul National University, Seoul, South Korea*
[b] *Department of Atmospheric Science, Kongju National University, Kongju, South Korea*
[c] *Department of Atmospheric Sciences, University of Illinois at Urbana–Champaign, Urbana, Illinois*
[d] *School of Urban and Environmental Engineering, Ulsan National Institute of Science and Technology, Ulsan, South Korea*
[e] *Department of Environmental Planning, Graduate School of Environmental Studies, Seoul National University, Seoul, South Korea*

(Manuscript received 30 November 2020, in final form 2 September 2021)

ABSTRACT: This study identifies diverse synoptic weather patterns of warm-season heavy rainfall events (HREs) in South Korea. The HREs not directly connected to tropical cyclones (TCs) (81.1%) are typically associated with a midlatitude cyclone from eastern China, the expanded North Pacific high, and strong southwesterly moisture transport in between. They are frequent both in the first (early summer) and second rainy periods (late summer) with impacts on the south coast and west of the mountainous region. In contrast, the HREs resulting from TCs (18.9%) are caused by the synergetic interaction between the TC and meandering midlatitude flow, especially in the second rainy period. The strong south-southeasterly moisture transport makes the southern and eastern coastal regions prone to the TC-driven HREs. By applying a self-organizing map algorithm to the non-TC HREs, their surface weather patterns are further classified into six clusters. Clusters 1 and 3 exhibit a frontal boundary between the low and high with differing relative strengths. Clusters 2 and 5 feature an extratropical cyclone migrating from eastern China under different background sea level pressure patterns. Cluster 4 is characterized by the expanded North Pacific high with no organized negative sea level pressure anomaly, and cluster 6 displays a development of a moisture pathway between the continental and oceanic highs. Each cluster exhibits a distinct spatiotemporal occurrence distribution. The result provides useful guidance for HRE prediction by depicting important factors to be differently considered depending on their synoptic categorization.

KEYWORDS: Convective storms/systems; Synoptic climatology; Extreme events; Monsoons; Rainfall

1. Introduction

In South Korea, approximately 66% of annual precipitation and 90% of heavy rainfall events (HREs) are concentrated from June to September (Fig. 1a). During the last three decades (1973–2005), annual precipitation in South Korea has increased, largely caused by the increase in frequency and intensity of warm-season HREs (Jung et al. 2011). Further increases in HRE frequency and intensity are expected under climate change scenarios (Cha et al. 2016; Kim et al. 2018). In the summer of 2020, South Korea experienced record-breaking monsoon rainfall with flash floods across the country due to consecutive HREs (Park et al. 2021a). Considering that HREs exert substantial socioeconomic impacts, understanding their climatological and dynamic/thermodynamic features is highly important.

The warm-season HREs in South Korea (hereafter, simply HREs unless otherwise specified) are significantly influenced by the East Asian summer monsoon (EASM). In general, the EASM becomes pronounced as the North Pacific high (NPH; also known as the western North Pacific subtropical high) expands toward the east coast of the Asian continent, which allows southwesterly monsoon flow along its northern boundary. The early part of the EASM is often characterized by a thousand-kilometer-long rainband developing along the quasi-stationary monsoon front (Ninomiya 1984; Kodama 1992; Wang et al. 2001; Wang and LinHo 2002; Chen et al. 2004). Late in the EASM, the EASM rainfall becomes dominated by tropical cyclones (TCs) and midlatitude frontal activities, as the western ridge of the NPH shifts eastward due to the developing monsoon trough (Wang and LinHo 2002; Chen et al. 2004; Guo et al. 2017). These two distinct phases of the EASM produce a well-known bimodal rainfall distribution over East Asia (Wang and LinHo 2002; Chen et al. 2004), which is also evident in Korea (Fig. 1a).

In a more regional sense, the Korean summer monsoon—a subsystem of the EASM known as "changma"—is affected by five air masses with differing thermodynamic characteristics: 1) the maritime tropical air mass centered over the subtropical western North Pacific; 2) the monsoon tropical air mass related to the intertropical convergence zone; 3) the continental tropical air mass over central China, 4) the continental polar air mass from Siberia, and 5) the maritime polar air mass from the Okhotsk Sea (Fig. 1b; Lee et al. 2017). For example, the quasi-stationary monsoon front and related rainfall are typically considered to be the result of a clash between these air masses, especially, maritime tropical and maritime polar air

---

Supplemental information related to this paper is available at the Journals Online website: https://doi.org/10.1175/MWR-D-20-0388.s1.

Corresponding author: Joowan Kim, joowan.k@gmail.com

DOI: 10.1175/MWR-D-20-0388.1

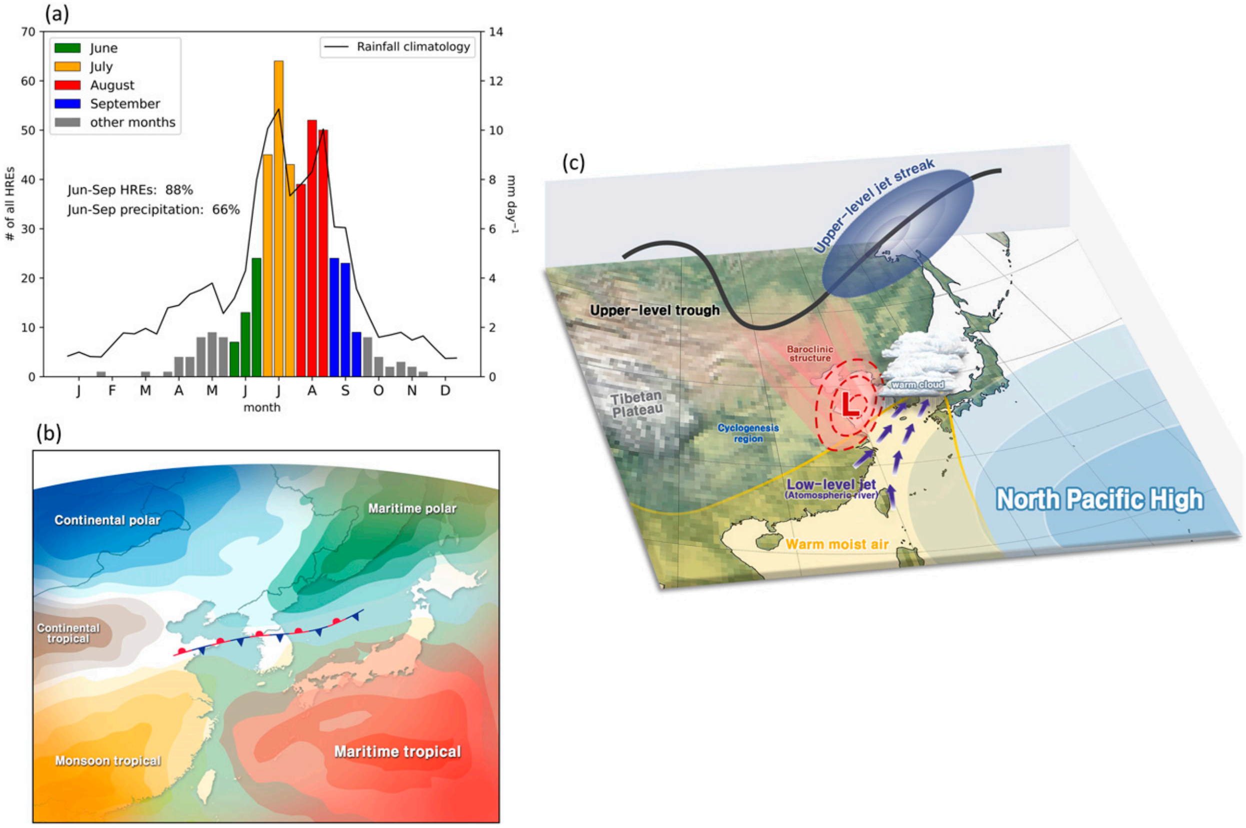

FIG. 1. (a) The number of all HREs in 10-day bins over the period of 1979–2018 (colored bars) overlaid with rainfall climatology (mm day^{-1}, black line). The 57 weather stations are considered. See section 2b for the HRE definition. (b) Schematic representation of the five warm-season air masses around the Korean Peninsula and quasi-stationary monsoon front. (c) Schematic illustration of the synoptic condition of the HREs in South Korea.

masses (Tomita et al. 2011; Seo et al. 2015; Kawasaki et al. 2021). According to Seo et al. (2015), the air mass perspective provides a useful framework to understand summer rainfall variability in East Asia.

Nevertheless, the HREs have finer synoptic-scale structures that cannot be purely explained by air mass variability. They often accompany a southwesterly low-level jet, which brings a large amount of moisture, and an entrance region of an upper-level jet, which induces upward motion on the equatorward side via a thermally direct secondary circulation (Lee et al. 2008a,b). Recently, Park et al. (2021b) revealed that the vertically organized baroclinic system, i.e., an upper-level trough coupled to a surface cyclone, is a key synoptic factor of the HREs. Based on quasigeostrophic (QG) dynamics, they concluded that dynamic uplift associated with the HREs is primarily forced by a baroclinically deepening trough in the upper-to-middle troposphere. The role of geostrophic frontogenesis around the upper-level jet entrance, which is responsible for the thermally direct secondary circulation, turned out to be relatively minor.

Other important characteristics of the HREs involve their thermodynamic properties. The HREs generally occur through the warm-cloud processes with ample moisture (Sohn et al. 2013; Hamada and Takayabu 2018) supported by a plume of tropospheric moisture transport, i.e., an atmospheric river (Kamae et al. 2017; Park et al. 2021c; Ryu et al. 2021). This allows the HREs to occur under the moist adiabatic near-neutral condition and to have only a low-to-moderate amount of convective available potential energy (CAPE), which is generally smaller than that of the deep convective thunderstorms over the U.S. Great Plains (Hong 2004; Sohn et al. 2013), although similarly low-CAPE flooding events have been also reported in the United States (e.g., Schumacher and Johnson 2008).

The general synoptic conditions of the HREs have been extensively studied as summarized in Fig. 1c. However, no study has explored the potential diversity of the associated synoptic weather patterns. Although Lee and Kim (2007) classified the HREs, their analysis relied on a subjective categorization of mesoscale morphologies of precipitation systems. Jo et al. (2020) objectively classified the localized HREs, but their analysis was only statistically based in relation to spatiotemporal characteristics. In China and Japan, the typical synoptic weather patterns related to HREs have been objectively classified (e.g., Ohba et al. 2015; Nguyen-Le et al. 2017; Zhao et al. 2019), but such analysis is still lacking for the Korean HREs.

This study aims to provide essential explanations for the HREs. By sampling the June–September HREs for 1979–2018, the HREs resulting from TCs (TC-HREs) and those not directly connected to TCs (non-TC HREs) are separately analyzed. By applying a self-organizing map (SOM) clustering analysis to the non-TC HREs, their six distinct weather patterns are further identified. The synoptic characteristics of the TC-HREs, non-TC HREs and their six clusters are elaborated.

The remainder of this paper is organized as follows: section 2 discusses the data and methodology. Section 3 investigates and compares the non-TC HREs and TC-HREs. Section 4 details the six clusters of the non-TC HREs. Last, results are summarized and further discussion is given in section 5.

2. Data and methods

a. Data

Hourly precipitation data from the Korea Meteorological Administration (KMA) Automated Synoptic Observing System (ASOS) are used to identify the HREs. Excluding stations on Jeju Island due to the different regional climate from mainland Korea (Lee 1999), a total of 57 ASOS stations with continuous observations from 1979 to 2018 are used.

Meteorological variables from the European Centre for Medium-Range Weather Forecasts (ECMWF) interim reanalysis (ERA-Interim; Dee et al. 2011) are used to analyze the HREs' synoptic features. The ERA-Interim data are obtained at 6-h intervals with a 1.5° × 1.5° horizontal grid spacing and 37 pressure levels. For all datasets, only June–September is considered to focus on the warm-season HREs. Anomaly fields are calculated by subtracting the 40-yr 6-h climatology.

b. HRE definition

The warm-season HREs are identified following the definition in Park et al. (2021b). The HRE is defined as an event with ≥110 mm of rainfall in 12 h at any single ASOS station, which corresponds to the KMA criteria for an HRE warning. If HREs are observed multiple times at several stations within 12 h, the HRE with the largest 12-h accumulated rainfall is selected to discard redundant HREs with same synoptic environment. As a result, a total of 392 events are identified for 1979–2018, accounting for 88% of all-season HREs (Fig. 1a). The reference time of each HRE is defined as the center of the 12-h window for the maximum 12-h accumulated rainfall (e.g., 0600 UTC for the maximum 12-h accumulated rainfall during 0000–1200 UTC).

The HREs concurrent with TCs near the Korean Peninsula (TC-HREs) are considered separately. These events are determined by analyzing TC best tracks provided by the Regional Specialized Meteorological Center–Tokyo Typhoon Center. Following the KMA criteria (KMA 2011), the HRE is considered to be a direct result of the TC if a TC is located within the domain of 32°–40°N, 120°–138°E without transitioning to an extratropical cyclone. The TC tracks associated with the TC-HREs are shown in Fig. 2. In general, the TCs recurve over the East China Sea before approaching the Korean Peninsula.

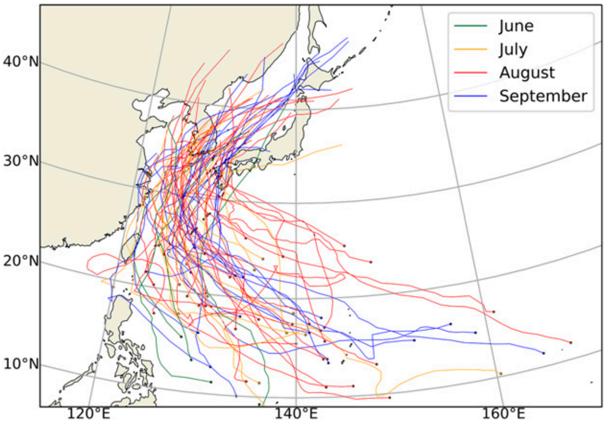

FIG. 2. Tracks of TCs involved in the TC-HREs with different colors depending on months. For clarity, tracks for the grades of tropical depression (before becoming TC) and extratropical cyclone (after extratropical transition) are not expressed. The closed circles denote the genesis location of TCs.

The non-TC HREs and TC-HREs account for 81.1% (318 events) and 18.9% (74 events) of the total warm-season HREs. As summarized in Table 1, the maximum 12-h accumulated rainfall of the TC-HREs is about 30 mm greater than that of the non-TC HREs. The duration is also about 3 h longer in the TC-HREs. However, those differences fall within their respective one standard deviation, suggestive of substantial event-by-event spreads. Hereafter, the non-TC HREs are simply referred to as the HREs.

c. SOM analysis applied to the HREs

The SOM algorithm is used to analyze the diverse surface weather patterns associated with the HREs. As such, the SOM is a type of artificial neural network that reduces high-dimensional data into a manageable low-dimensional array of nodes based on the Euclidean distance through iterative training (Kohonen 1998, 2013). It accommodates nonlinearities within the dataset without assuming orthogonality between clusters (Reusch et al. 2005; Rousi et al. 2015). Furthermore, the SOM technique does not require any prior knowledge of the expected results, as it is based on unsupervised learning. These features of the SOM algorithm enable it to produce a reliable and objective summary of the data.

Node arrangement is a crucial parameter in SOM clustering analysis. In general, applying excessive nodes causes fewer input data to be sorted into each node, leading to a loss of generality. In contrast, adopting too few nodes results in severe overfitting of the input data with less accuracy. To ascertain the optimal node arrangement, statistical methods have been considered (e.g., Johnson 2013; Rousi et al. 2015; Liu et al. 2016). However, a trial-and-error approach has also been popular to obtain more interpretable and physically meaningful results (e.g., Nigro and Cassano 2014; Ohba et al. 2015; Jung et al. 2019).

We use mean sea level pressure (SLP) fields 6 h before the reference time (hereafter, simply ''−6 h'') as the clustering

TABLE 1. Summary of the HREs and TC-HREs. The first three rows are synoptic description, and preferred occurrence period and region. The fourth and fifth rows are averages of the maximum 12-h accumulated rainfall amount (mm) among the 57 ASOS stations and HRE duration (h) with their one standard deviation. The sixth through eighth rows represent the magnitude, and zonal and meridional components of **IVT** (kg m^{-1} s^{-1}) with their one standard deviation. The last four rows are ω (Pa s^{-1}), and ratios of ω to ω_{QG}, ω_{Dyn} to ω_{Dia}, and ω_n to ω_s at 500 hPa. The values in the last seven rows are estimated in the mature stage (0 h) over the boxed region in the right panel of Fig. 3b for the HREs and Fig. 6b for the TC-HREs.

	HREs (81.1%)	TC-HREs (18.9%)
Synoptic description	Migrating cyclone with northwestward expansion of the NPH	Synergetic interaction between TC and midlatitude flow
Preferred period	First and second rainy periods	Second rainy period
Preferred region	South coast and west of mountainous region	South and east coasts
Max12-h rainfall	170.7 ± 60.9	198.0 ± 82.0
HRE duration	15.3 ± 10.4	18.2 ± 12.5
|**IVT**|	449.8 ± 181.2	706.2 ± 304.2
Zonal **IVT**	292.0 ± 194.6	−101.2 ± 277.9
Meridional **IVT**	240.6 ± 166.0	378.5 ± 357.0
ω	−0.16	−0.25
$\omega:\omega_{QG}$	1:1.00	1:0.99
$\omega_{Dyn}:\omega_{Dia}$	1:1.69	1:2.55
$\omega_n:\omega_s$	1:1.79	1:1.00

property, because the SLP effectively summarizes surface weather conditions on a synoptic weather chart. The considered domain is 27°–47°N, 112°–136°E. For the node array, a 1 × 6 array is selected based on the following rationale: the one-dimensional array can result in more clearly distinguished clusters due to the self-organizing nature of the SOM that locates similar clusters adjacently (Kohonen 1998). More importantly, a one-dimensional array is desirable as it forces the nodes to be arranged in a sequence that can be reflective of the subseasonal variation in the background SLP fields (i.e., from early to late summer), allowing a more physically interpretable result. After multiple sensitivity tests with different node sizes systematically varying in only one dimension ($1 \times n$), six nodes are found to be ideal for summarizing the surface weather patterns of the HREs. Other SOM parameters follow the suggestions of Liu et al. (2006) and are summarized in the online supplemental material Table S1.

d. Diagnosis of vertical motion

By solving the Q-vector-form QG omega equation (see appendix A), vertical motions by dynamic and diabatic processes, which are referred to as ω_{Dyn} and ω_{Dia}, respectively, are quantified. Here, vertical motion due to the beta effect is not addressed as it is very weak on the synoptic-scale motion. The nature of ω_{Dyn} is further examined by decomposing the Q vector into the transverse and shearwise components. The resulting vertical motions are referred to as ω_n and ω_s, respectively. By definition, the transverse and shearwise Q vectors are the Lagrangian measures for the magnitude and direction changes of the potential temperature gradient following the geostrophic wind, respectively. The former is often associated with the confluent/diffluent motion around the jet entrance/exit region and responsible for the transverse (i.e., cross-frontal) secondary circulation. In contrast, the latter is typically generated by undulating baroclinic waves (i.e., trough). Further details and their application to weather analyses can be found in the literature (e.g., Keyser et al. 1992; Martin 1999, 2006, 2007; Moore et al. 2019; Park et al. 2021b). The numerical details of the QG omega equation inversion are in compliance with those in Park et al. (2021b).

3. Climatology of the HREs and TC-HREs

a. Synoptic characteristics of the HREs

In this section, the synoptic characteristics of the HREs are investigated through a composite analysis. Figure 3a shows the temporal evolution of the SLP, its anomaly, relative vorticity at 850 hPa and vertically integrated water vapor transport (**IVT**; see appendix B) at −36, −18, and 0 h. Here, the relative vorticity is smoothed at a T42 resolution to focus on the synoptic-scale disturbances. At −36 h, the NPH expands northwestward, and a negative SLP anomaly appears over eastern China. The negative SLP anomaly continues to deepen and propagate northeastward. At 0 h, it develops into a well-defined surface cyclone with an intensity of ~2 cyclonic vorticity units (CVU ≡ 10^{-5} s^{-1}), enhancing the southwesterly **IVT** on its leading edge.

Figure 3b shows the temporal evolution of the 250-hPa geopotential height (HGT) and wind speed, as well as the 500-hPa vertical motion. The upper-level flow meanders in time with a deepening trough and strengthening jet streak. Note that the upper-level trough is located immediately west of the surface cyclone, suggestive of its baroclinic development. At 0 h, South Korea is positioned on the east of the trough and the equatorward side of the jet entrance, which is a favorable condition for upward motion (see blue contours).

Figure 4 shows the result of the QG omega equation inversion for the mature HREs. The ω_{Dia} is stronger than ω_{Dyn}, especially

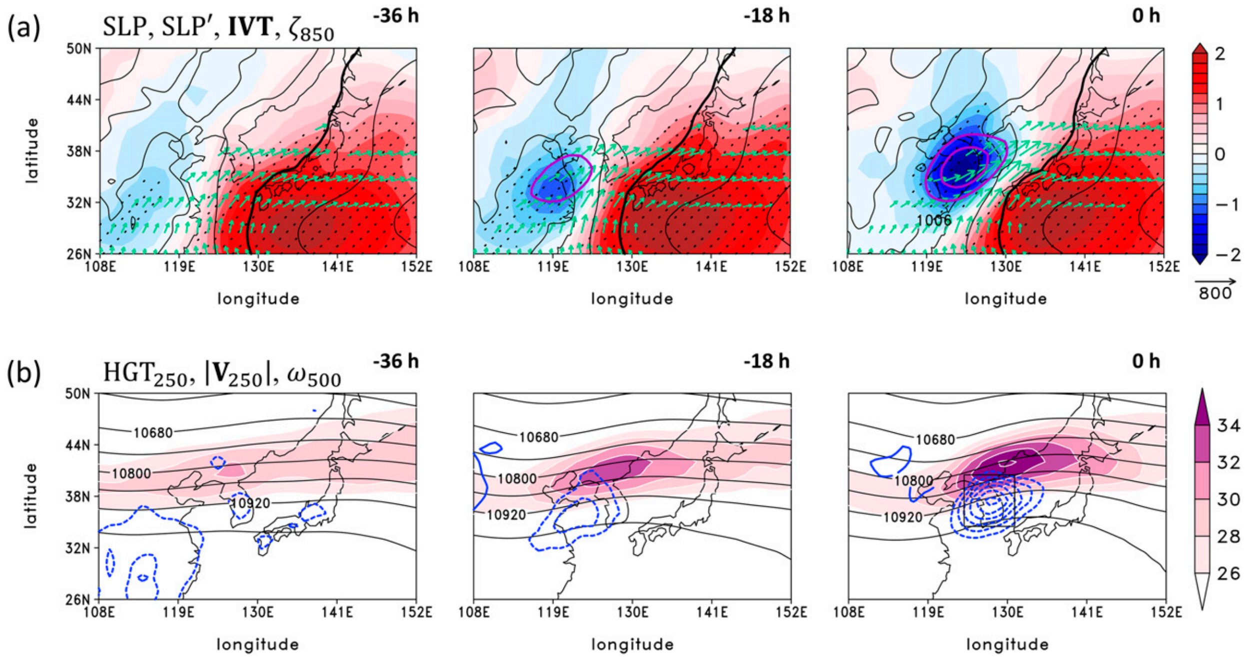

FIG. 3. Time evolution (−36, −18, and 0 h) of synoptic circulation patterns of the HREs: (a) SLP (hPa, contoured in black), SLP anomalies (hPa, shaded), **IVT** (kg $\mathrm{m^{-1}\,s^{-1}}$, vectors >300 kg $\mathrm{m^{-1}\,s^{-1}}$), and the 850-hPa relative vorticity truncated to a T42 resolution (contoured in purple with a 1-CVU interval starting from 1 CVU), and (b) HGT (gpm, contoured in black) and wind speed ($\mathrm{m\,s^{-1}}$, shaded) at 250 hPa, and vertical velocity at 500 hPa (Pa $\mathrm{s^{-1}}$, contoured in blue with a 0.04 Pa $\mathrm{s^{-1}}$ interval). In (a), the 1010-hPa contour is highlighted in bold. The SLP anomalies are stippled when statistically significant at the 95% confidence level based on a two-tailed Student's *t* test. In (b), the boxed region in the right panel denotes the core of the 500-hPa ascent.

in the middle-to-lower troposphere (1.7 times stronger at 500 hPa; Fig. 4a). This highlights a critical role of the latent heat release during the HRE, especially through the warm-cloud processes (Sohn et al. 2013; Hamada and Takayabu 2018). Unlike ω_{Dia}, ω_{Dyn} is maximized at the upper troposphere (~350 hPa). The ω_s is dominant over ω_n throughout troposphere (1.8 times stronger at 500 hPa; Fig. 4b), which implies that rotation of the isentropes by the trough plays a more important role than geostrophic frontogenesis around the jet entrance in generating ω_{Dyn}.

The lower- and upper-level circulation patterns and vertical motion mechanisms of the HREs were also recently analyzed in Park et al. (2021b). Figure 5 provides further synoptic details of the mature HREs. At 850 hPa, a horizontal gradient of equivalent potential temperature (θ_e) is pronounced around the Korean Peninsula (Fig. 5a). This θ_e gradient appears to be established partly by the advection of warm moist air through the southwesterly **IVT** (see Fig. 3a). The Petterssen's frontogenesis function (see appendix B) clearly shows that the frontogenesis occurs along the large θ_e gradient (blue contours). In the vertical, θ_e exhibits a moist-adiabatically unstable condition in the boundary layer, especially to the south (Fig. 5b). The free troposphere, however, shows a near-neutral or only weakly unstable condition. This condition may be favorable for convective instability in the near-surface level and further self-maintenance of the convection in the free troposphere, which can significantly amplify the HREs. The specific humidity over South Korea is higher than over the subtropics in nearly the entire troposphere (blue contours), which facilitates the successive diabatic enhancement of the HREs. This free-tropospheric high specific humidity has been also reported for the Japanese HREs (Hamada and Takayabu 2018). Possibly, the deep omega profile established by the bottom-heavy ω_{Dia} and top-heavy ω_{Dyn} distributions (see Fig. 4a) may contribute to this condition through an upward moisture supply throughout the troposphere.

The HGT anomalies exhibit a westward-tilted vertical structure with dual minima in the upper and lower troposphere. A rising motion is evident between the negative and positive HGT anomalies, which is a well-known feature of a developing baroclinic system. On the equatorward side of the upper-level jet core, horizontal wind divergence collocates with the near-surface convergence beneath (Fig. 5d), which may facilitate the thermally direct secondary circulation (Lee et al. 2008b) and its further contribution to the low-level frontogenesis through a semigeostrophic feedback (Yuan et al. 2020).

b. Synoptic characteristics of the TC-HREs

Figure 6 shows the synoptic evolution of the TC-HREs. The TC is generally located over the East China Sea at −36 h and moves poleward along the western boundary of the NPH in time (Fig. 6a; see also Fig. 2). In the mature stage of the TC-HREs (0 h), the TC is positioned immediately southwest of the Korean Peninsula. At this time, cyclonic vorticity of the TC reaches ~6 CVU—3 times larger than the cyclone in the HREs (cf. Figs. 3a and 6a). Along the right side of the TC, a

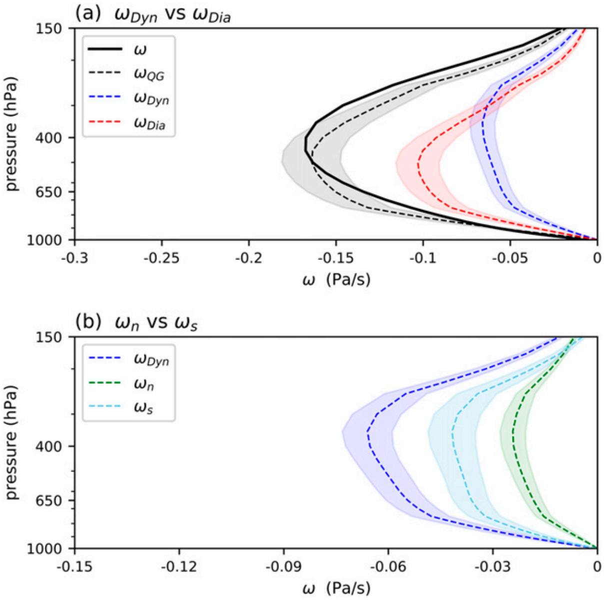

FIG. 4. (a) Vertical profiles of composited ERA-Interim omega (ω; black solid), QG omega (ω_{QG}; black dashed), dynamic omega (ω_{Dyn}; blue dashed), and diabatic omega (ω_{Dia}; red dashed) of the mature HREs (0 h). The values are averaged over the boxed region in the right panel of Fig. 3b. The 95% confidence interval is shaded based on a bootstrap test with 10 000 times resampling. (b) As in (a), but for the dynamic omega (ω_{Dyn}; blue dashed) and their two components: transverse omega (ω_n; green dashed) and shearwise omega (ω_s; sky-blue dashed).

large amount of moisture is transported toward Korea as manifested by south-southeasterly **IVT**.

In the upper troposphere, a trough–ridge couplet is found in midlatitudes (Fig. 6b). On the top of the ridge, the upper-level jet develops, placing its entrance region to the north of the Korean Peninsula. Although the upper-level jet accelerates in time, the trough–ridge couplet stays in place with no eastward propagation. This synoptic configuration induces a well-organized region of ascent over South Korea at −36 and −18 h, which is well separated from the direct impact of the TC (i.e., eyewall convection; see blue contours). Given the abundant moisture remotely fed by the TC, this midlatitude ascent may cause predecessor rainfall events before the TC arrives (e.g., Galarneau et al. 2010; Byun and Lee 2012; Baek et al. 2015). In the mature stage (0 h), the TC convection merges with the midlatitude ascent, generating a more rigorous uplift over South Korea. The amplification of the upper-level flow from −36 to 0 h is likely supported by a diabatic outflow of the predecessor rainfall events and TC (Grams and Archambault 2016). Accordingly, the TC-HREs could be explained by the result of synergetic interaction between TCs and nearby midlatitude baroclinic waves. This is indeed a typical feature of the transitioning TCs in baroclinic zones (Evans et al. 2017; Keller et al. 2019).

Although a contribution of centrifugal force, which can be large in the high-curvature flow, is neglected in the QG omega equation (Moore and Vanknowe 1992), ω_{QG} successfully reproduces the reanalyzed omega for the mature TC-HREs (Fig. 7a). The upward motion is stronger than that of the HREs (cf. Figs. 4a and 7a), primarily due to the stronger ω_{Dia}. Note that ω_{Dia} is 2.6 times stronger than ω_{Dyn} at 500 hPa. This is consistent with Quinting and Jones (2016) who reported that dry dynamics accounts for only a third of the ascent during extratropical transition over the western North Pacific. For ω_{Dyn}, ω_s is stronger than ω_n in the lower troposphere, but ω_n becomes comparable to or slightly stronger than ω_s in the upper-to-middle troposphere (Fig. 7b). This suggests that geostrophic frontogenesis is comparably important in the upper-to-middle troposphere, while rotation of isentropes is more important in the lower troposphere.

Further dynamic/thermodynamic details of the mature TC-HREs are shown in Fig. 8. At 850 hPa, a tongue of the high θ_e stretching from south to north is observed (Fig. 8a) due to the southerly dominant **IVT** (see also Fig. 6a). Along the northern side of the high θ_e tongue, strong frontogenesis occurs, particularly over the Korean Peninsula (blue contours). As in the HREs, the vertical structure of θ_e shows convectively unstable condition in the boundary later and near-neutral condition in the free troposphere (Fig. 8b), but θ_e is overall larger than that in the HREs (cf. Figs. 5b and 8b).

As in the HREs, the HGT anomalies exhibit a westward tilted vertical structure (Fig. 8c), representing the transitioning TC. However, the negative HGT anomalies in the lower troposphere are stronger than those in the upper troposphere, which manifests a warm-core nature of the TC. This is also consistent with the dominant ω_s over ω_n only in the lower troposphere (see Fig. 7b). On the equatorward side of the upper-level jet core, upper-level divergence and lower-level convergence are well collocated with stronger magnitudes than those in the HREs (cf. Figs. 5d and 8d). In particular, the strong poleward cross-jet flow is evident in the upper troposphere, which is consistent with the fact that the diabatic outflow of the transitioning TC significantly contributes to the downstream flow amplification (Grams and Archambault 2016).

c. *Spatiotemporal occurrence distributions of the HREs and TC-HREs*

The HREs and TC-HREs are clearly distinguished also by their spatiotemporal occurrence distributions. Figures 9a,b show their temporal occurrence distributions in 10-day bins. The HREs have two frequency peaks, which is consistent with the climatological first (late June–July) and second rainy periods (mid-August–mid-September) (Fig. 9a). In contrast, the TC-HREs are more frequent in the second rainy period (Fig. 9b). This is consistent with the fact that the western North Pacific TC activity is more pronounced in late summer than early summer (Chen et al. 2004; Guo et al. 2017).

Figures 9c,d present the spatial occurrence distributions of the HREs and TC-HREs across the 57 ASOS stations. Both the HREs and TC-HREs are frequently observed along the south coast. However, they show sharp differences related to the north–south-oriented mountains. While the HREs preferentially occur in the western side of the mountainous areas, the TC-HREs are largely confined to the east coast. This difference can be explained by the different direction of moisture transport between the HREs versus TC-HREs. As summarized in Table 1, the HREs are often accompanied by the southwesterly **IVT** impinging on the western slope of the mountains (see also

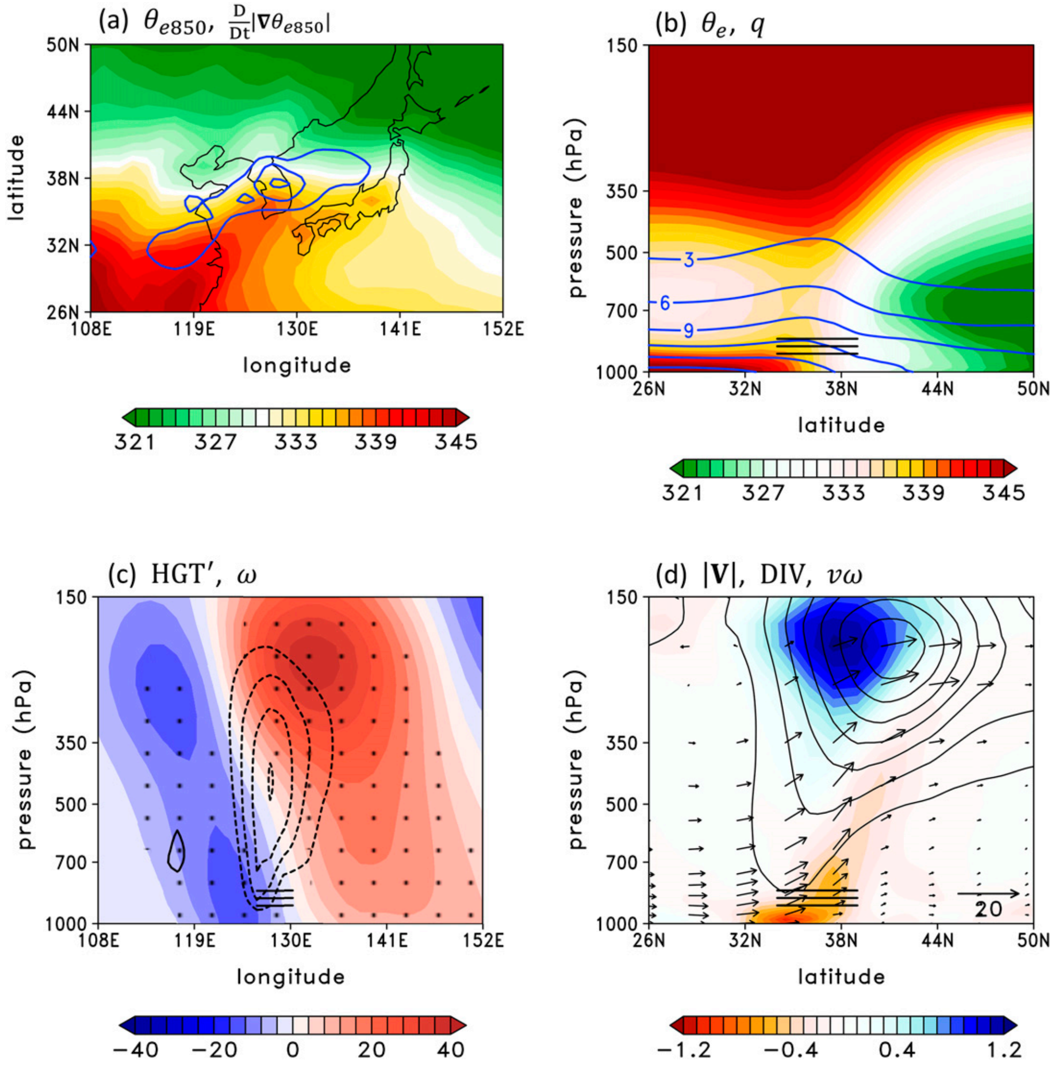

FIG. 5. Thermodynamic and dynamic structures of the mature HREs (0 h): (a) 850-hPa θ_e (K, shaded) and the Petterssen frontogenesis function applied to the 850-hPa θ_e [contoured in blue for positive values with a 1 K (100 km day)$^{-1}$ interval], (b) latitude–pressure cross section of θ_e (K, shaded) and specific humidity (g kg^{-1}, contoured), (c) longitude–pressure cross section of HGT anomalies (gpm, shaded) and vertical velocity (contoured with a 0.04 Pa s^{-1} interval), and (d) latitude–pressure cross section of wind speed (contoured with a 4 m s^{-1} interval starting from 12 m s^{-1}), horizontal mass divergence (10^{-5} s^{-1}, shaded), and meridional–vertical wind (m s^{-1}, vectors; vertical velocity is multiplied by an aspect ratio of −32.72). In (b)–(d), the plotted variables are longitudinally or latitudinally averaged over the boxed region in the right panel of Fig. 3b. The three horizontal lines in (b)–(d) indicate the approximate location of South Korea. In (c), the HGT anomalies are stippled when statistically significant at the 95% confidence level based on a two-tailed Student's t test.

Fig. 3a). In contrast, the south-southeasterly **IVT** in the TC-HREs is favorable for moisture convergence and orographic lifting on eastern edge of the mountains (see also Fig. 6a).

4. Six clusters of the HREs

a. *Overview of the SOM clustering results*

The SOM algorithm is applied to the 318 HREs to find their potentially diverse surface weather patterns. Figure 10 presents the SOM result—SLP fields at −6 h over the clustering domain composited for the six clusters (C1–C6). Due to the self-organizing nature of the SOM, the result shows continuous SLP patterns with adjacent clusters. Note that closer to C1, a more pronounced low SLP appears, but approaching C6, a high SLP becomes dominant.

Although slight differences are found in intensity and duration between the six clusters, those differences fall within their respective one standard deviation (Table 2). However, those clusters are well differentiated by their spatiotemporal

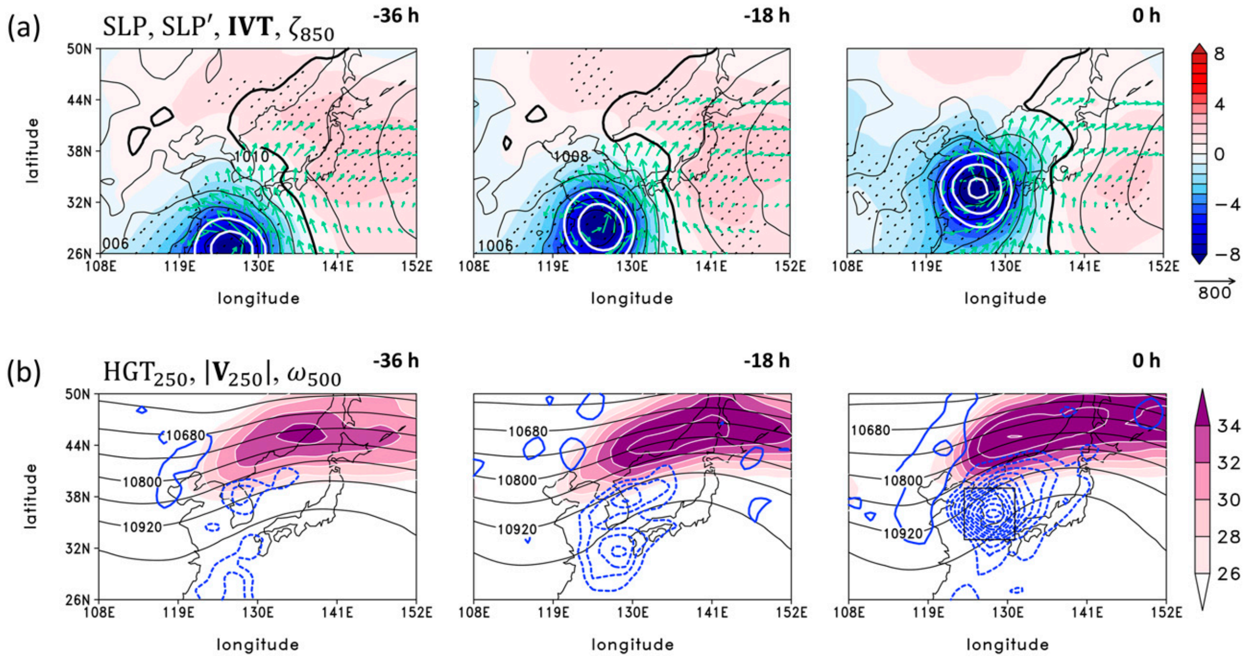

FIG. 6. As in Fig. 3, but for the TC-HREs. In (a), the 850-hPa T42 relative vorticity is contoured in white with a 2-times-larger interval than in Fig. 3a (2-CVU interval). Note that the shading range in (a) is 4 times larger than that in Fig. 3a.

occurrence distributions (Fig. 11). Moving from left to right across the clusters, the preferred occurrence period tends to shift from the early to late summer (Fig. 11a). For instance, C1 and C3 peak in July while C5 and C6 favor August and September, respectively. In contrast, C2 and C4 exhibit bimodal frequency peaks with a tail to the left. This gradual transition in the temporal distribution from C1 to C6 can be anticipated from the use of the one-dimensional node array due to the self-organizing nature of the SOM. Differences are also found in their spatial distributions (Fig. 11b). While C1 predominantly occurs in the western side of the elevated terrain, C6 is largely confined to the southwest coast. C3 and C4 are also frequent in the western half of the country, but its extent is less distinct than C1. C2 and C5 are relatively spread across the country.

b. Synoptic patterns for each cluster

The synoptic circulation patterns of the six HRE clusters are described in Figs. 12–17 in the same format as Fig. 3. To facilitate discussion, the clusters that share common features are grouped together. For example, the synoptic background of C1 and C3 can be explained as a quasi-stationary frontal boundary between low and high SLPs, while C2 and C5 feature a direct influence from an extratropical cyclone.

The inversion result of the QG omega equation is provided for all clusters as supplemental material in the same format as Fig. 4 (Figs. S1, S3, S5, S7, S9, and S11). In all clusters, diabatic uplift (i.e., ω_{Dia}) is greater than dynamic uplift (i.e., ω_{Dyn}), especially in the middle-to-lower troposphere as in the total HREs. Similarly, ω_{Dyn} is more associated with shearwise ascent (i.e., ω_s) rather than transverse counterpart (i.e., ω_n) throughout the troposphere.

The dynamic/thermodynamic details are also given for all clusters as supplemental material in the same format as Fig. 5 (Figs. S2, S4, S6, S8, S10, and S12). In all clusters, the vertical structure of θ_e features a favorable condition for convective instability as in the total HREs. However, the horizontal distribution of θ_e at 850 hPa and the vertical structure of HGT

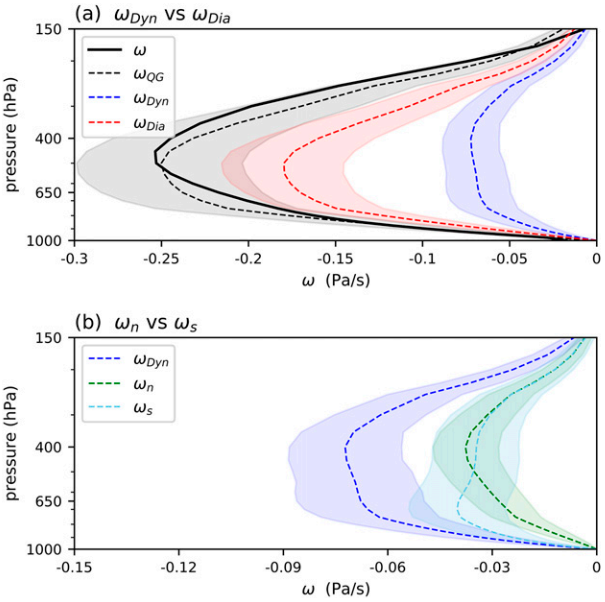

FIG. 7. As in Fig. 4, but for the TC-HREs. The values are averaged over the boxed region in the right panel of Fig. 6b.

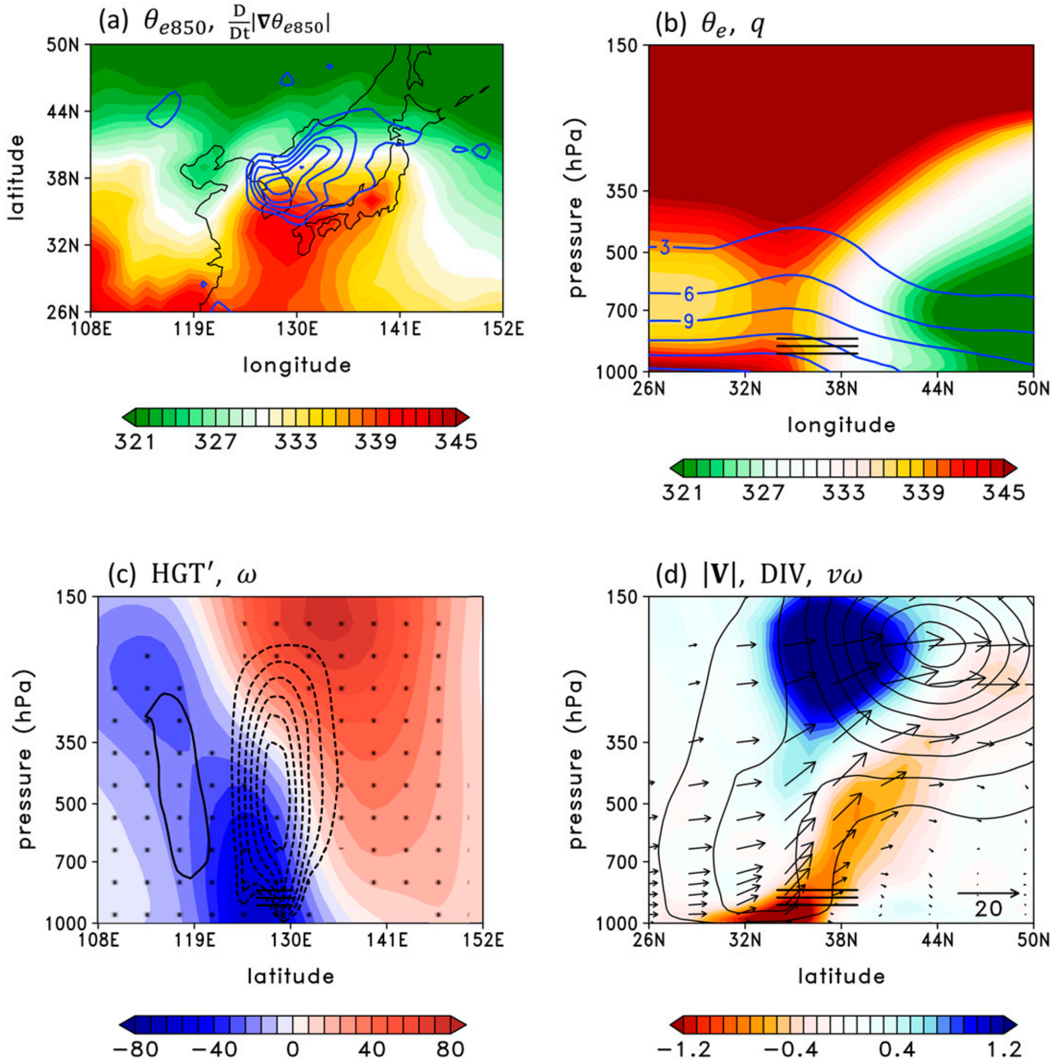

FIG. 8. As in Fig. 5, but for the TC-HREs. Note that the shading range in (c) is 2 times larger than that in Fig. 5c.

anomaly differ between clusters in association with their distinct surface weather patterns.

1) C1 AND C3: QUASI-STATIONARY FRONTAL BOUNDARY BETWEEN LOW AND HIGH

C1 and C3 account for approximately 39.6% of the HREs. They are characterized by a region of low SLP over northeastern China (north of the Korean Peninsula) and high SLP over the northwestern Pacific, forming a quasi-stationary frontal zone in between (Figs. 12a and 13a). The frontogenetic activity is evident along the large low-level θ_e gradient (Figs. S2a and S4a). However, C1 and C3 are differentiated by the relative strengths of the lows and highs. While C1 is characterized by a stronger low with a relatively weak high (Fig. 12a), C3 features somewhat comparable strengths of low and high (Fig. 13a). This background difference is likely associated with the differing seasonal march of the NPH, as manifested by the 1010-hPa isobar (cf. thick black lines in Figs. 12a and 13a).

In both clusters, a strong southwesterly **IVT** develops along the frontal boundary from −36 h. This moisture transport further intensifies in time, significantly affecting the western side of the Korean Peninsula (Fig. 11b). The **IVT** in this HRE group is largest in magnitude compared to other clusters. The transient increase in **IVT** can be explained by a secondary development of the cyclone along the frontal boundary. At −36 h, a cyclonic vorticity core appears over eastern China (see white and purple contours in Figs. 12a and 13a, respectively). This early disturbance (~1 CVU) travels along the frontal boundary with continuous intensification to ~2–3 CVU at 0 h. Note that the frontal cyclone is well separated from the quasi-stationary cyclonic core over northeastern China. This feature reflects the importance of multiscale interactions between the quasi-stationary pressure systems and the transient frontal cyclones in setting the stage for the HREs.

Figures 12b and 13b illustrate the upper-level circulation of C1 and C3, respectively. In both clusters, the upper-level trough develops and propagates eastward in time, phasing

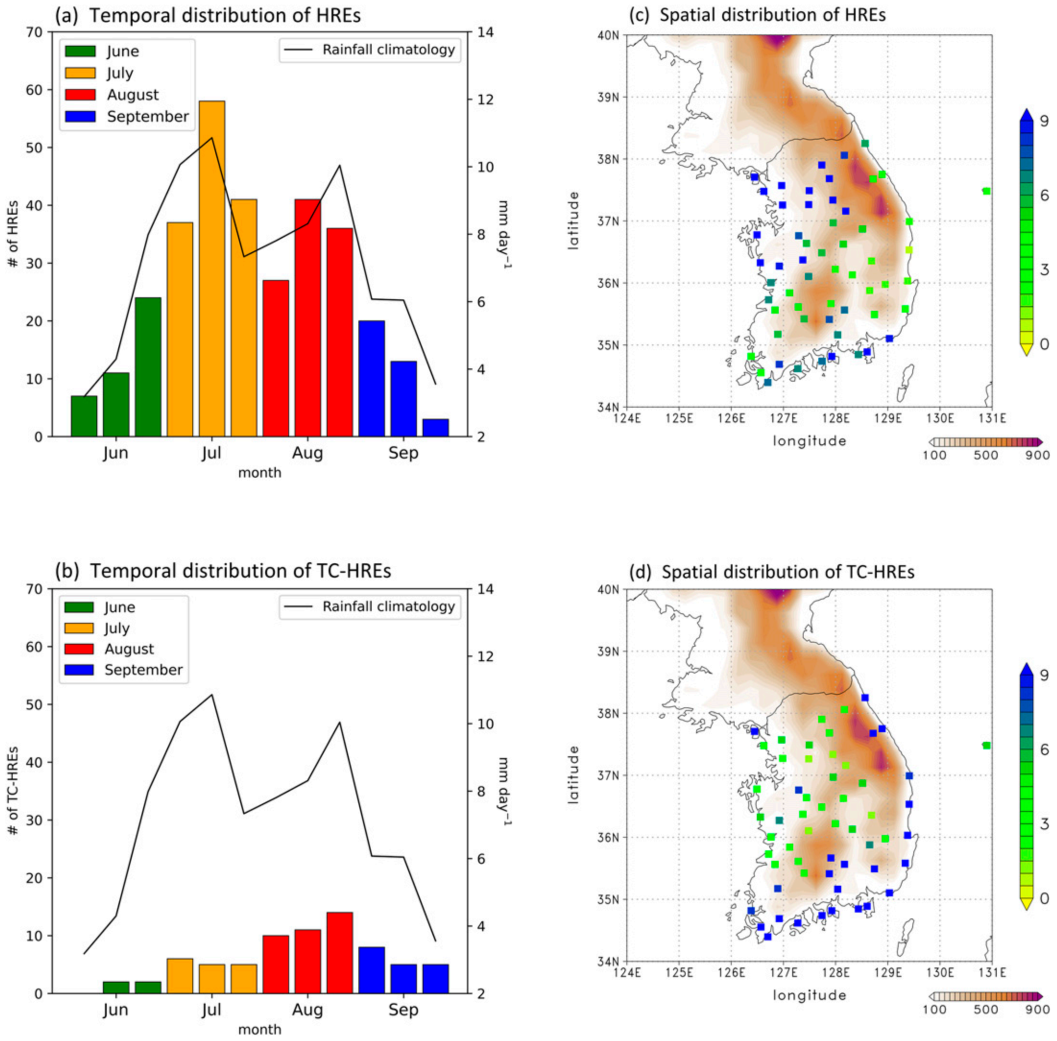

FIG. 9. (left) The number of the (a) HREs and (b) TC-HREs in 10-day bins from June to September (colored bars) overlaid with rainfall climatology (mm day^{-1}, black line). (right) Spatial distributions of the probability of occurrence of the (c) HREs and (d) TC-HREs (%, colored squares) overlaid with terrain (m, shaded). The probability of occurrence means the conditional probability that a given ASOS station records HRE when HRE occurs in South Korea.

with the surface frontal cyclone. On the eastern side of the trough, the midlevel ascent is well organized. However, C1 and C3 are somewhat different in the location of the upper-level trough and jet streak. The trough in C1 comes from the northwest of the Korean Peninsula, and the jet streak develops along the base of the trough (Fig. 12b). In contrast, the trough in C3 comes from the west of the Korean Peninsula, and the relatively weaker jet streak organizes on the east of the trough axis (Fig. 13b). In both clusters, ω_s is greater than ω_n (Figs. S1b and S3b), implying an important role of the isentropes rotation by the trough in dynamically forced uplift (i.e., ω_{Dyn}).

2) C2 AND C5: EXTRATROPICAL CYCLONE FROM EASTERN CHINA

C2 and C5 account for approximately 28.9% of the HREs and represent the direct impact of an extratropical cyclone. At −36 h, a weak cyclone with an intensity of 1 CVU appears over eastern China (Figs. 14a and 15a). This early stage cyclone (~1 CVU) continues to intensify as it propagates northeastward, especially when encountering the Yellow Sea at −18 h. In the mature stage (0 h), the cyclone is located immediately west of the Korean Peninsula with an intensity of ~3 CVU. The cyclone has a westward tilted structure in the vertical (Figs. S6c and S8c), which is a typical feature of baroclinic instability. Unlike C1 and C3 in which the large-scale pressure systems preinduce southwesterly **IVT**, the cyclones in C2 and C5 by themselves produce substantial **IVT**. The **IVT** exhibits stronger southerly components than westerly components, which likely results in the less skewed HRE occurrences toward the western side of the country compared to C1 and C3 (Fig. 11b).

Despite the similar extent of intensification (~3 CVU at 0 h), the cyclone in C2 tends to deepen more than the one in C5

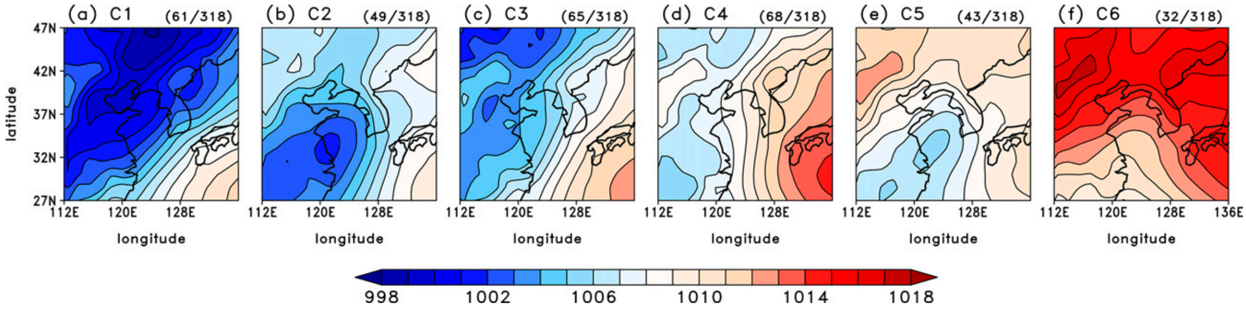

FIG. 10. The results of the 1 × 6 SOM clustering applied to the HREs. The plotted variable is the composited −6-h SLP fields for the 6 clusters (C1–C6) over the clustering domain (27°–47°N, 112°–136°E).

(cf. blue shadings in Figs. 14a and 15a). This indicates that both the SLP and relative vorticity need to be carefully monitored in forecasting the extratropical cyclone-induced HREs in Korea. Another noticeable difference is the background SLP. While C2 is dominated solely by the well-deepened extratropical cyclone (Fig. 14a), C5 is also characterized by the background high SLP (and its positive anomalies) over the Asian continent and the northwestern Pacific Ocean (Fig. 15a). This likely explains why the cyclone in C5 has comparable cyclonic vorticity to that in C2 despite the relatively weak negative SLP anomaly. The high SLP surrounding the cyclone can contribute to the increased pressure gradient around the cyclone and thus to the strong cyclonic vorticity.

Figures 14b and 15b depict similar upper-level flows to each other. The upper-level trough deepens and propagates eastward from the west, which is consistent with the developing surface cyclone. The upper-level jet streak also develops on the east of the trough with its entrance region to the north of South Korea at 0 h. This upper-level configuration provides a favorable condition for dynamically forced uplift (i.e., ω_{Dyn}). The strong 500-hPa upward motion is evident in the east of the trough and the equatorward side of the jet entrance. Comparison of ω_n and ω_s implies that the rotating effect by the trough is more important than geostrophic frontogenesis around the jet entrance in generating ω_{Dyn} for both clusters (Figs. S5b and S7b). However, the relative contribution of ω_n is greater in C5 possibly due to the stronger upper-level jet (cf. shadings in Figs. 14b and 15b), which may force stronger frontogenetic confluence on the entrance region.

3) C4: LOCAL DISTURBANCE AT THE EDGE OF THE NPH

C4 composes approximately 21.4% of the HREs. This HRE type is dominated by a high pressure anomaly centered southeast of Korea (Fig. 16a). This anomalous high is interpreted as the expanded NPH toward the Korean Peninsula (see the 1010-hPa isobar). In contrast to the previous clusters, the surface weather pattern is nearly invariant in time with no organized low pressure anomaly. Instead, the expanded NPH induces strong southwesterly **IVT** along its northwestern boundary, affecting the western part of South Korea (Fig. 11b). At 0 h, a region of weak transient cyclonic

TABLE 2. As in Table 1, but for the six HRE clusters. The values in the last seven rows are estimated at 0 h over the boxed region in the right panel of Fig. 3b.

	C1 (19.2%)	C3 (20.4%)	C2 (15.4%)	C5 (13.5%)	C4 (21.4%)	C6 (10.0%)
Synoptic description	Quasi-stationary frontal boundary between low and high		Extratropical cyclone from eastern China		Local disturbance at the edge of the NPH	Moisture pathway between continental and oceanic highs
Preferred period	First rainy period		First and second rainy periods	Second rainy period	First and second rainy periods	Second rainy period
Preferred region	West of mountainous region		Indistinct preferred region		West of mountainous region	Southwest coast
Max12-h rainfall	186.8 ± 89.8	170.6 ± 52.7	163.1 ± 41.5	163.9 ± 53.6	172.8 ± 56.1	161.4 ± 45.6
HRE duration	16.7 ± 11.0	14.0 ± 9.0	15.8 ± 10.5	16.0 ± 14.1	15.5 ± 8.8	13.1 ± 8.3
|**IVT**|	502.2 ± 173.4	436.4 ± 170.3	359.0 ± 134.1	415.1 ± 140.2	359.0 ± 134.1	328.0 ± 148.3
Zonal **IVT**	358.2 ± 156.5	198.7 ± 195.2	178.8 ± 172.1	275.1 ± 141.1	178.8 ± 172.1	176.2 ± 169.5
Meridional **IVT**	269.2 ± 177.5	255.0 ± 184.4	196.7 ± 156.3	243.1 ± 142.5	196.7 ± 156.3	187.7 ± 137.3
ω	−0.17	−0.23	−0.15	−0.14	−0.15	−0.16
$\omega:\omega_{\mathrm{QG}}$	1:1.00	1:1.02	1:1.12	1:0.98	1:1.12	1:1.19
$\omega_{\mathrm{Dyn}}:\omega_{\mathrm{Dia}}$	1:2.27	1:1.65	1:1.35	1:1.69	1:1.35	1:1.40
$\omega_n:\omega_s$	1:1.88	1:2.07	1:1.66	1:1.68	1:1.66	1:1.32

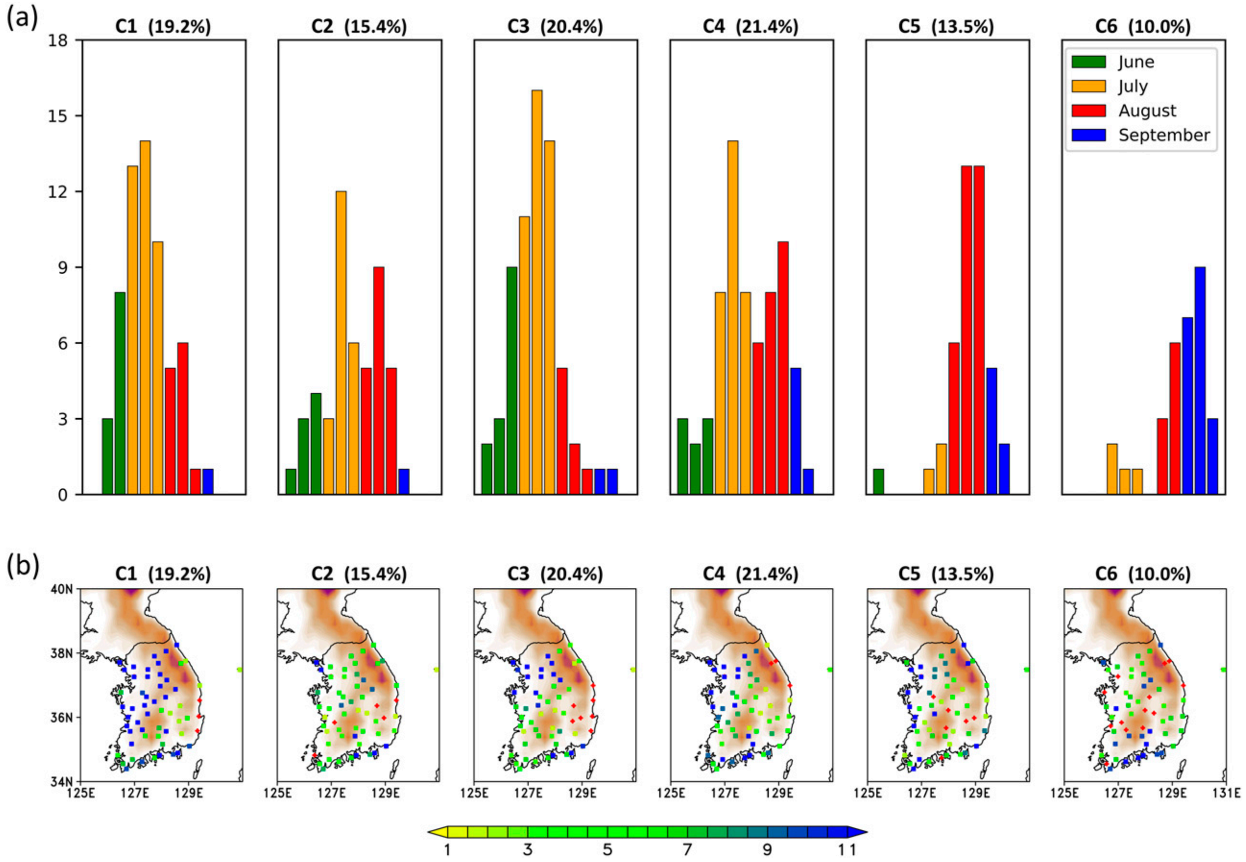

FIG. 11. As in Fig. 9, but for the six HRE clusters. In (b), the ASOS stations where no HRE was observed are marked by red dots.

vorticity (~1 CVU) is observed over the Yellow Sea. The absence of negative SLP anomalies and the sudden appearance of relatively weak cyclonic vorticity imply that the C4-type HREs are triggered by a local disturbance on the NPH boundary. Perhaps, the C4-type HREs are not likely well forecasted based on traditional synoptic analysis, and higher-resolution analysis would be required to investigate and forecast such events.

In the upper troposphere, the weak upper-level trough and jet streak are found, but they are nearly stationary without propagation or strengthening in time (Fig. 16b). This is consistent with the nearly invariant SLP pattern in Fig. 16a. Indeed, this HRE type exhibits a nearly barotropic vertical structure (Fig. S10c), implying no interaction between the upper and lower troposphere. Nevertheless, the QG omega equation inversion reveals that ω_{Dyn} plays a nonnegligible role in upward motion over South Korea (Fig. S9a), with a larger contribution of ω_s than ω_n (Fig. S9b).

4) C6: MOISTURE PATHWAY BETWEEN CONTINENTAL AND OCEANIC HIGHS

The C6-type HREs mostly occur in late August and September (Fig. 11a). They are characterized by overwhelmingly high SLP (and its positive anomalies) over the Asian continent and the northwestern Pacific (Fig. 17a). Although C6 has the smallest fraction with only 10.0%, this pattern consistently appears in the SOM sensitivity tests, which implies that C6 is neither a statistical artifact nor a random collection of events. From −36 to −18 h, moisture transport occurs between the continental and oceanic highs but mostly over the East China Sea. At 0 h, however, the southwesterly **IVT** reaches Korea with a sudden development of the surface trough between the two large-scale surface highs. The cyclonic vorticity over the surface trough is quite strong (~2 CVU), building the moisture pathway toward Korea from the East China Sea. We found that various systems are occasionally involved (e.g., remote effect of TCs, meso-α- to synoptic-scale cyclone, local instability, etc.), implying a necessity of a more case-by-case investigation beyond this background-based classification.

At −36 h, a weak upper-level trough is observed far upstream (Fig. 17b). The trough continuously deepens while propagating eastward. At 0 h, the trough is located immediately west of Korea with the downstream upper-level jet whose entrance region is positioned to the north of Korea. Note that the upper-level jet in C6 is strongest compared to other clusters, possibly due to the increased surface baroclinicity in late summer

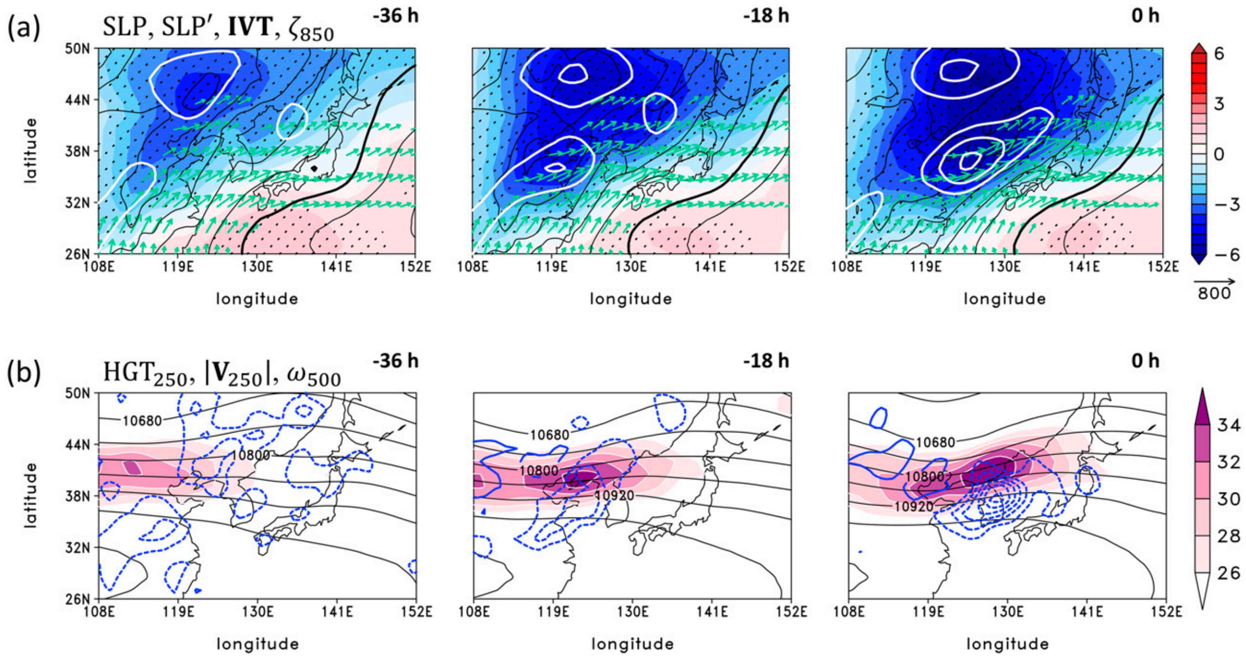

FIG. 12. As in Fig. 3, but for the C1-type HREs. The 850-hPa T42 relative vorticity in (a) is contoured in white. Note that the shading range in (a) is 3 times larger than that in Fig. 3a.

(Fig. S12a). In the east of the upper-level trough and south of the jet entrance, the strong ascent is organized. This implies a contribution from the dynamically forced ascent (i.e., ω_{Dyn}) to the development of the surface trough and HREs (see Fig. S11a). As in other clusters, ω_s is greater than ω_n (Fig. S11b), but the relative contribution of ω_n to ω_{Dyn} is largest in C6 (see also Table 2). This is possibly due to the strongest upper-level jet which may allow the strongest frontogenetic confluence on its entrance region.

5. Summary and discussion

This study examines the diverse synoptic weather patterns of the warm-season HREs in South Korea for 1979–2018. The

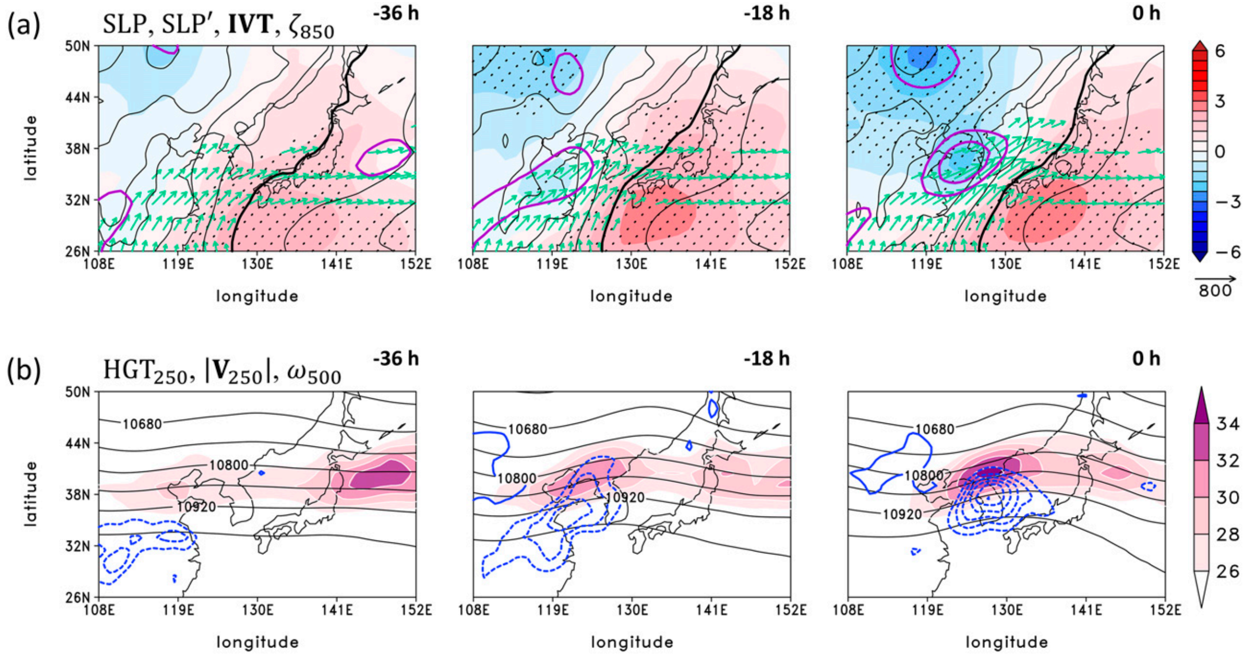

FIG. 13. As in Fig. 3, but for the C3-type HREs. Note that the shading range in (a) is 3 times larger than that in Fig. 3a.

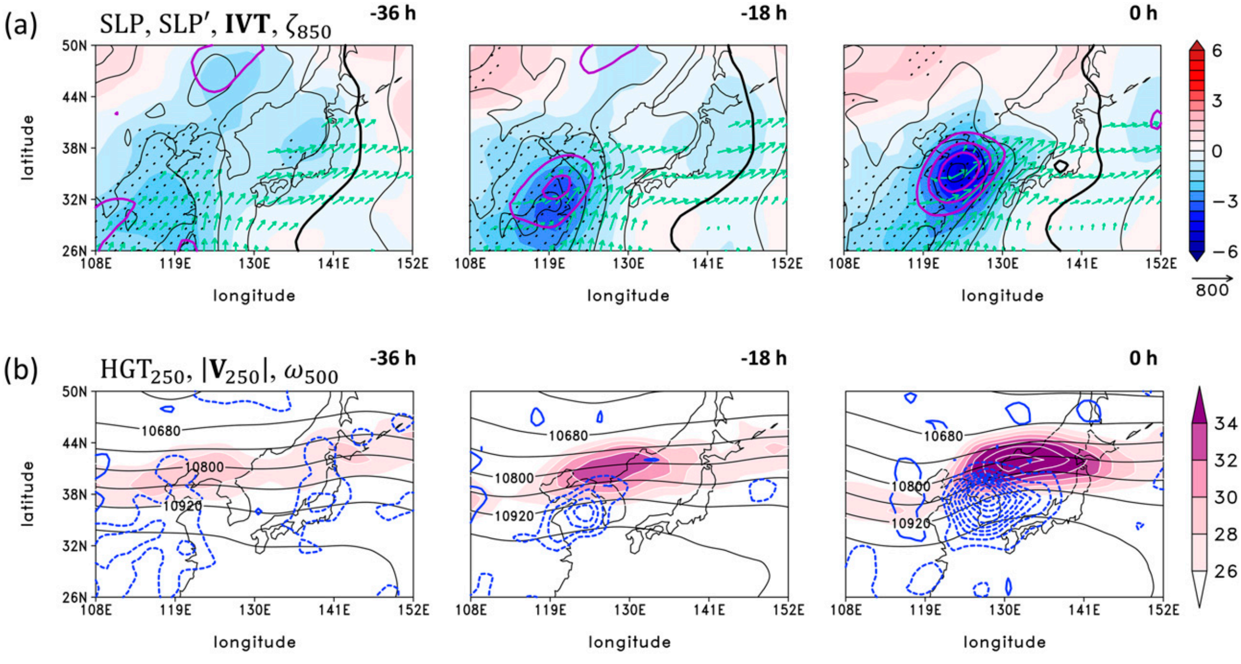

FIG. 14. As in Fig. 3, but for the C2-type HREs. Note that the shading range in (a) is 3 times larger than that in Fig. 3a.

HREs not directly connected to TCs (simply, HREs) and those resulting from TCs (TC-HREs) are analyzed separately. They can be summarized as follows (see also Table 1):

- *HREs (81.1%)*: A migrating surface cyclone from eastern China and a northwestward expansion of the NPH induces strong southwesterly moisture transport toward the Korean Peninsula. In the upper troposphere, a trough and jet streak develop in the west and north of South Korea, providing a favorable condition for ω_{Dyn}. The QG omega equation reveals that in the mature stage, ω_{Dia} is stronger than ω_{Dyn}, and rotation of the isentropes by the trough plays a dominant role in ω_{Dyn} ($\omega_s > \omega_n$). The atmosphere is moist-adiabatically

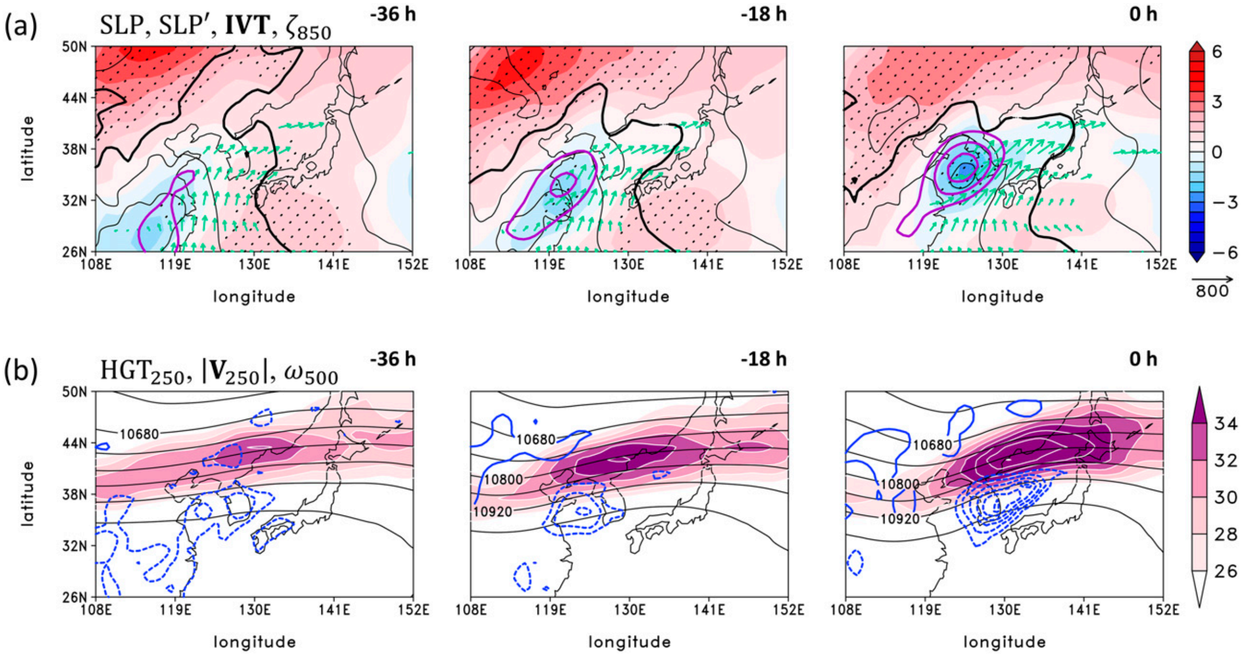

FIG. 15. As in Fig. 3, but for the C5-type HREs. Note that the shading range in (a) is 3 times larger than that in Fig. 3a.

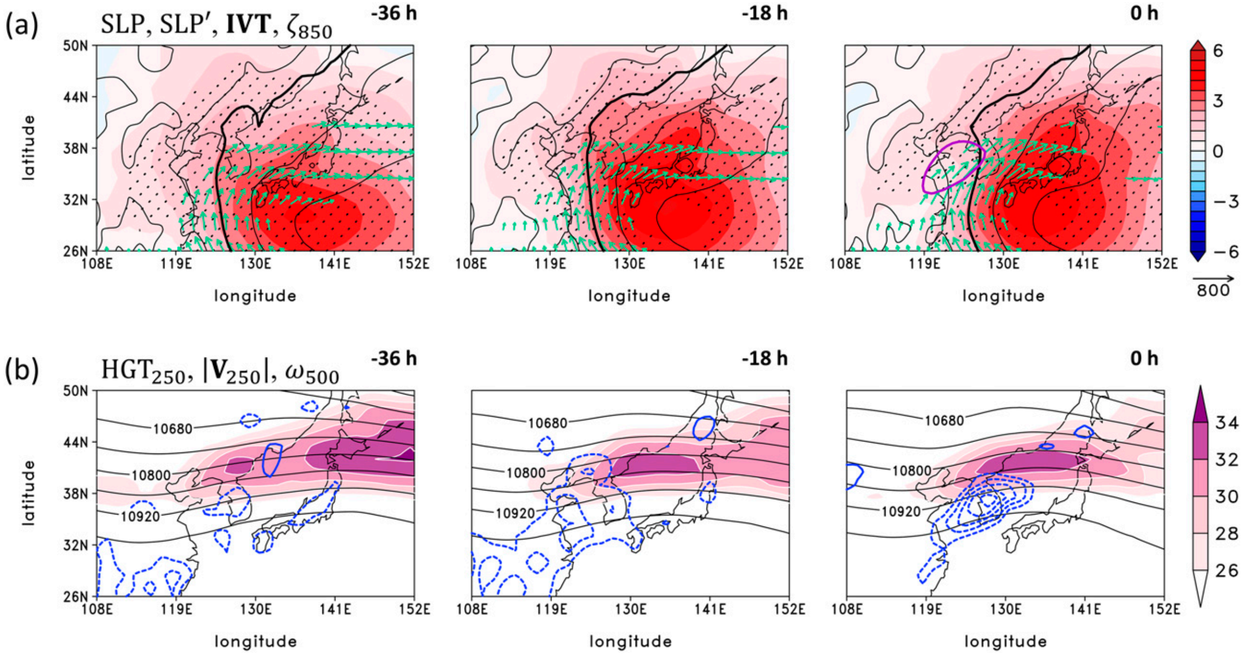

FIG. 16. As in Fig. 3, but for the C4-type HREs. Note that the shading range in (a) is 3 times larger than that in Fig. 3a.

unstable in the boundary layer but near-neutral in the free troposphere. The HREs are frequent both in the first and second rainy periods along the south coast and west of the north–south-oriented mountains.

- *TC-HREs (18.9%)*: The TC-HREs are characterized by phasing and synergetic interaction between a TC and midlatitude baroclinic flows. An upward motion often develops over South Korea even before the TC arrives, suggestive of predecessor rainfall events. In the mature stage, the TC is located immediately southwest of the Korean Peninsula with tremendous south-southeasterly moisture transport and highly amplified upper-level flow. According to the QG omega equation, ω_{Dia} is greater than ω_{Dyn} to a greater extent than in the HREs. Although ω_s is stronger than ω_n in the lower troposphere, ω_n becomes comparable to ω_s in the upper-to-middle troposphere, signifying the TC's warm-core nature experiencing strong geostrophic frontogenesis in the upper troposphere. The TC-HREs favor the second rainy period along the south and east coasts.

By applying a SOM algorithm to SLP of the HREs, the six distinct surface weather patterns are further identified. They can be summarized as below (see also Table 2):

- *Quasi-stationary frontal boundary between low and high (C1 and C3; 39.6%)*: This HRE group is characterized by a continental low over northeastern China and an oceanic high corresponding to the NPH, resulting in a quasi-stationary frontal boundary in between. Strong southwesterly moisture transport and a frontal cyclone develop between two large-scale pressure systems. In C1, the low SLP anomaly is more pronounced than the high SLP anomaly, but their strengths are nearly comparable in C3.
- *Extratropical cyclone from eastern China (C2 and C5; 28.9%)*: This HRE group features an extratropical cyclone from eastern China, which develops via baroclinic instability. The cyclone produces strong moisture transport along its leading edge with a stronger southerly component. Although similar in cyclonic vorticity, the cyclone in C2 deepens more than that in C5. While C2 is characterized solely by the well-deepened cyclone, C5 is described also by the surrounding high SLP.
- *Local disturbance at the edge of the NPH (C4; 21.4%)*: This HRE type is dominated by the expanded NPH, which induces strong southwesterly moisture transport along its boundary. In the absence of a low pressure anomaly, the HREs are likely triggered by a local disturbance on the NPH boundary. Compared to other clusters, the daily synoptic weather map is nearly invariant in time.
- *Moisture pathway between continental and oceanic highs (C6; 10.0%)*: The background weather pattern is characterized by high SLPs over the Asian continent and the northwestern Pacific. In between, a surface trough develops, building a moisture transport pathway from the East China Sea toward Korea. With a well-defined upper-level trough and jet streak, various rainfall systems can be involved.

In all clusters, the upper-level trough and jet streak are present, although their strength and/or location slightly differ. The QG omega equation reveals that in all clusters ω_{Dia} is greater than ω_{Dyn} with ω_s dominating over ω_n, although their relative contributions vary across the clusters. While C1 and C3 favor the first rainy period, C5 and C6 prefer the second rainy period. C2 and C4 frequently occur both in the first and second rainy periods. Spatially, C1, C3, and C4 mainly occur in the western half of the elevated terrain, while C6 are biased in the

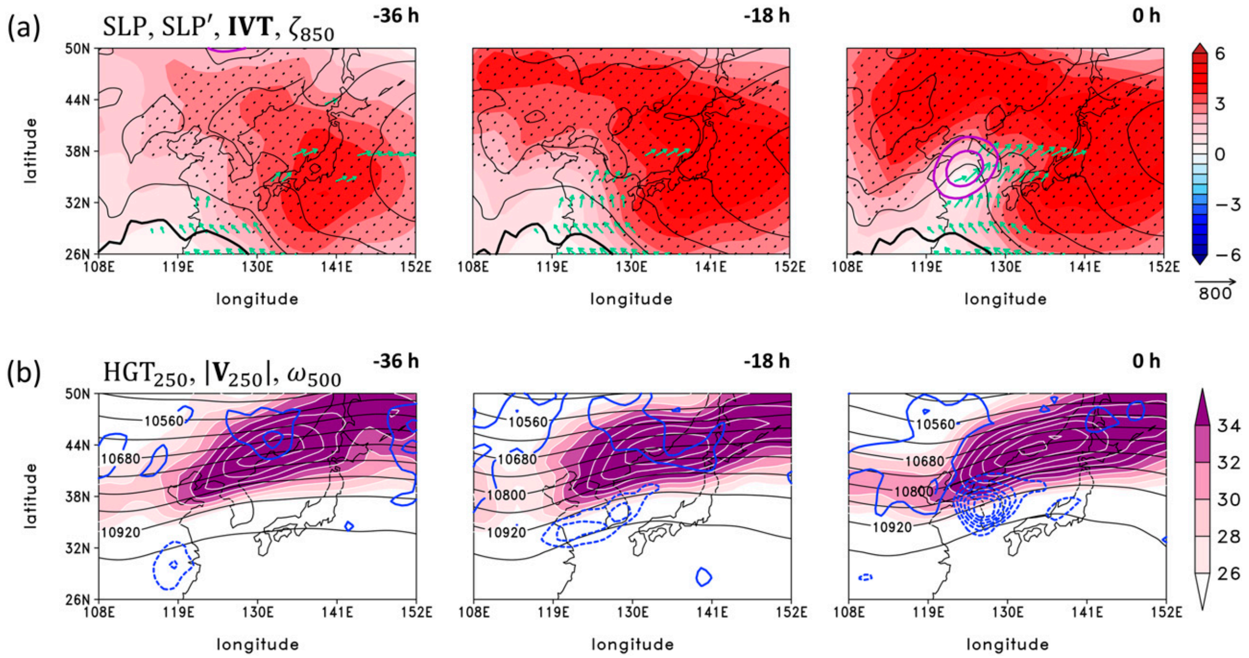

FIG. 17. As in Fig. 3, but for the C6-type HREs. Note that the shading range in (a) is 3 times larger than that in Fig. 3a.

southwest coast of the country. C2 and C5 exhibit no distinct occurrence region compared to other clusters.

This study suggests different forecasting factors depending on the HRE types. For the TC-HREs, for instance, both a TC and midlatitude baroclinic wave need to be considered because their synergetic interaction greatly contributes to vigorous upward motion. For the C1- and C3-type HREs, a frontal cyclone should be carefully monitored, because it has a substantial local cyclonic vorticity although the cyclone is not clearly distinguished in the background SLP fields. For the C2- and C5-type HREs, both the SLP and low-level relative vorticity need to be considered because the extratropical cyclone can strongly intensify (i.e., large cyclonic vorticity) despite only weakly deepened SLP (e.g., C5). To better predict the C4-type HREs, traditional synoptic analysis may be insufficient because there is no spatially organized disturbance. Instead, a higher-resolution model with well-tuned physical parameterizations is likely necessary. The C6-type HREs accompany a strongly amplified upper-level trough and jet, and thus it should be noted that various rainfall systems can develop in the given background synoptic state.

Beyond the SLP fields, other properties are also available in SOM clustering to examine different aspects of the HREs. For example, the dynamic tropopause could be an option if the upper-level modulation of the HREs is of interest (e.g., Agel et al. 2019). In fact, the upper-tropospheric disturbance often transiently modulates the East Asian summer rainfall (Horinouchi 2014; Horinouchi and Hayashi 2017; Park et al. 2021b). Identifying the diverse upper-tropospheric patterns and their differing dynamical impacts on surface weather conditions will shed additional light on the HRE dynamics and remains as a subject of future work.

The synoptic background patterns described in this study are based on composite analysis. Because the rainfall itself tends to be localized in nature (Jo et al. 2020), this approach has a limitation in presenting detailed local features of individual rainfall systems. Particularly, the C6-type HREs bear various rainfall systems within the given background SLP pattern. The large event-by-event spreads in intensity and duration of the HREs (Table 2) are still an open issue. While this study provides useful synoptic guideline for the HREs, detailed features of individual rainfall systems should be further investigated because their movement, spatiotemporal scale and development of subsynoptic-scale features can considerably determine the local rainfall rate and its duration (Doswell et al. 1996). In fact, the HREs are often related to various mesoscale systems embedded in the synoptic-scale flow (Sun and Lee 2002; Lee and Kim 2007; Shin et al. 2019). Given the multiscale nature of the HREs, extending this study to the favorable mesoscale systems will possibly offer a more detailed tool for weather forecasters and is left for future work.

Acknowledgments. We are grateful for the constructive comments of the three anonymous reviewers, which significantly improved this article. This work was funded by Korea Meteorological Administration Research and Development Program ‘‘Enhancement of Convergence Technology of Analysis and Forecast on Severe Weather’’ under Grant KMA2018-00121. This work was also supported by the National Research Foundation of Korea (NRF) grant funded by the Korea government (Ministry of Science and ICT) (NRF-2018R1A5A1024958).

Data availability statement. The KMA ASOS data are available at https://data.kma.go.kr/data/grnd/selectAsosRltmList.do?pgmNo=36. The TC best track data are available at https://www.jma.go.jp/jma/jma-eng/jma-center/rsmc-hp-pub-eg/trackarchives.html. The ERA-Interim data are available at https://apps.ecmwf.int/datasets/data/interim-full-daily/levtype=pl/.

APPENDIX A

Q-Vector-Form QG Omega Equation

The Q-vector-form QG omega equation (Hoskins and Pedder 1980; Holton 2004) is formulated as follows:

$$\left(\sigma_0\nabla^2 + f_0^2\frac{\partial^2}{\partial p^2}\right)\omega = -2\nabla\cdot\mathbf{Q} + f_0\beta_0\frac{\partial v_g}{\partial p} - \frac{\kappa}{p}\nabla^2 J, \qquad \text{(A1)}$$

where $\nabla^2 = \partial^2/\partial x^2 + \partial^2/\partial y^2$; $\nabla = (\partial/\partial x)\mathbf{i} + (\partial/\partial y)\mathbf{j}$; $\mathbf{i}$ and $\mathbf{j}$ are the unit vectors in the zonal and meridional directions, respectively. The σ_0 is the area-averaged and event-averaged static stability parameter. The three terms on the right-hand side are the dynamic, beta, and diabatic forcings, respectively.

The $\mathbf{Q}$ denotes the Q vector. The Coriolis parameter f_0 and its meridional gradient β_0 are evaluated at 38°N; v_g is the meridional geostrophic wind speed. The κ is R_d/C_{pd}, where R_d and C_{pd} are the dry gas constant and the specific heat of dry air at constant pressure, respectively; $J = C_{\mathrm{pd}}\dot{T}_{\mathrm{Dia}}$ is the diabatic heating rate per unit mass, where $\dot{T}_{\mathrm{Dia}}$ is the diabatic temperature tendency predicted by the ECMWF forecast model.

The Q vector is expressed in the Cartesian coordinate as follows:

$$\mathbf{Q} = -\gamma\left[\left(\frac{\partial\mathbf{V}_g}{\partial x}\cdot\nabla\theta\right)\mathbf{i} + \left(\frac{\partial\mathbf{V}_g}{\partial y}\cdot\nabla\theta\right)\mathbf{j}\right], \qquad \text{(A2)}$$

where γ is $(R_d/p)(p/1000\,\mathrm{hPa})^{\kappa}$; $\mathbf{V}_g$ and θ are the geostrophic wind and the potential temperature, respectively. Because the Q-vector convergence is dry dynamic forcing, Eq. (A2) can be rewritten under the adiabatic and nondivergent condition as follows:

$$\mathbf{Q} = \gamma\frac{D_g}{Dt}\nabla\theta, \qquad \text{(A3)}$$

where $D_g/Dt = \partial/\partial t + \mathbf{V}_g\cdot\nabla$ (Keyser et al. 1988, 1992). By considering the orientation of $\mathbf{Q}$ with respect to $\nabla\theta$, $\mathbf{Q}$ can be decomposed in a natural coordinate into the transverse ($Q_n\mathbf{n}$) and shearwise components ($Q_s\mathbf{s}$):

$$Q_n\mathbf{n} = \left(\gamma\frac{D_g}{Dt}|\nabla\theta|\right)\mathbf{n}, \qquad Q_s\mathbf{s} = \left(\gamma\frac{D_g}{Dt}\nabla\theta\cdot\mathbf{s}\right)\mathbf{s}. \qquad \text{(A4)}$$

Here, $\mathbf{n} = \nabla\theta/|\nabla\theta|$ is the cross-isentropic unit vector pointing to the warm air, and $\mathbf{s} = \mathbf{k}\times\mathbf{n}$ is the along-isentropic unit vector with warm air to the right. The Cartesian expression of Eqs. (A4) follows Park et al. (2021b). To remove synoptically unimportant features, $\mathbf{V}_g$ and θ are smoothed at a T42 spectral resolution before calculating $\mathbf{Q}$. The $\dot{T}_{\mathrm{Dia}}$ is also smoothed at a T128 spectral resolution.

APPENDIX B

Diagnostics for Moisture Transport and Frontogenesis

The moisture transport is evaluated using **IVT**, which is a flux-form water vapor transport vertically integrated from 1000 to 300 hPa:

$$\mathbf{IVT} = \left(-\frac{1}{g}\int_{1000\mathrm{hPa}}^{300\mathrm{hPa}} qu\,dp\right)\mathbf{i} + \left(-\frac{1}{g}\int_{1000\mathrm{hPa}}^{300\mathrm{hPa}} qv\,dp\right)\mathbf{j}, \qquad \text{(B1)}$$

where g is the gravitational acceleration; q is the specific humidity; u and v are the zonal and meridional winds, respectively.

The frontogenesis is evaluated using the 2D Petterssen's kinematic frontogenesis function (Petterssen 1936; Keyser et al. 1988) applied to θ_e:

$$F = \frac{D}{Dt}|\nabla\theta_e| = -\frac{1}{2}|\nabla\theta_e|(D - E\cos 2\beta), \qquad \text{(B2)}$$

where $D/Dt = \partial/\partial t + u\partial/\partial x + v\,\partial/\partial y$; $D = \partial u/\partial x + \partial v/\partial y$ is the horizontal mass divergence; $E = \sqrt{E_{\mathrm{st}}^2 + E_{\mathrm{sh}}^2}$ is the magnitude of total deformation, where $E_{\mathrm{st}} = \partial u/\partial x - \partial v/\partial y$ and $E_{\mathrm{sh}} = \partial v/\partial x + \partial u/\partial y$ are the stretching and shearing deformations, respectively. The angle $\beta = \delta - \alpha$ is defined as the difference between the angle of local orientation of the axis of dilatation, i.e., $\delta = (1/2)\arctan(E_{\mathrm{sh}}/\mathrm{E}_{\mathrm{st}})$, and that of the isentrope, i.e., $\alpha = \arctan[-(\partial\theta_e/\partial x)/(\partial\theta_e/\partial y)]$.

REFERENCES

Agel, L., M. Barlow, F. Colby, H. Binder, J. L. Catto, A. Hoell, and J. Cohen, 2019: Dynamical analysis of extreme precipitation in the US northeast based on large-scale meteorological patterns. *Climate Dyn.*, **52**, 1739–1760, https://doi.org/10.1007/s00382-018-4223-2.

Baek, E.-H., J.-H. Kim, J.-S. Kug, and G.-H. Lim, 2015: Midtropospheric frontogenesis associated with antecedent indirect precipitation ahead of tropical cyclones over the Korean Peninsula. *Tellus*, **67A**, 27476, https://doi.org/10.3402/tellusa.v67.27476.

Byun, K.-Y., and T.-Y. Lee, 2012: Remote effects of tropical cyclones on heavy rainfall over the Korean Peninsula—Statistical and composite analysis. *Tellus*, **64A**, 14983, https://doi.org/10.3402/tellusa.v64i0.14983.

Cha, D.-H., and Coauthors, 2016: Future changes in summer precipitation in regional climate simulations over the Korean Peninsula forced by multi-RCP scenarios of HadGEM2-AO. *Asia-Pac. J. Atmos. Sci.*, **52**, 139–149, https://doi.org/10.1007/s13143-016-0015-y.

Chen, T.-C., S.-Y. Wang, W.-R. Huang, and M.-C. Yen, 2004: Variation of the East Asian summer monsoon rainfall. *J. Climate*, **17**, 744–762, https://doi.org/10.1175/1520-0442(2004)017<0744:VOTEAS>2.0.CO;2.

Dee, D. P., and Coauthors, 2011: The ERA-Interim reanalysis: Configuration and performance of the data assimilation system. *Quart. J. Roy. Meteor. Soc.*, **137**, 553–597, https://doi.org/10.1002/qj.828.

Doswell, C. A., III, H. E. Brooks, and R. A. Maddox, 1996: Flash flood forecasting: An ingredients-based methodology. *Wea. Forecasting*, **11**, 560–581, https://doi.org/10.1175/1520-0434(1996)011<0560:FFFAIB>2.0.CO;2.

Evans, C., and Coauthors, 2017: The extratropical transition of tropical cyclones. Part I: Cyclone evolution and direct impacts. *Mon. Wea. Rev.*, **145**, 4317–4344, https://doi.org/10.1175/MWR-D-17-0027.1.

Galarneau, T. J., L. F. Bosart, and R. S. Schumacher, 2010: Predecessor rain events ahead of tropical cyclones. *Mon. Wea. Rev.*, **138**, 3272–3297, https://doi.org/10.1175/2010MWR3243.1.

Grams, C. M., and H. M. Archambault, 2016: The key role of diabatic outflow in amplifying the midlatitude flow: A representative case study of weather systems surrounding western North Pacific extratropical transition. *Mon. Wea. Rev.*, **144**, 3847–3869, https://doi.org/10.1175/MWR-D-15-0419.1.

Guo, L., N. P. Klingaman, P. L. Vidale, A. G. Turner, M. Demory, and A. Cobb, 2017: Contribution of tropical cyclones to atmospheric moisture transport and rainfall over East Asia. *J. Climate*, **30**, 3853–3865, https://doi.org/10.1175/JCLI-D-16-0308.1.

Hamada, A., and Y. N. Takayabu, 2018: Large-scale environmental conditions related to midsummer extreme rainfall events around Japan in the TRMM region. *J. Climate*, **31**, 6933–6945, https://doi.org/10.1175/JCLI-D-17-0632.1.

Holton, J. R., 2004: *An Introduction to Dynamic Meteorology*. 4th ed. Academic Press, 535 pp.

Hong, S.-Y., 2004: Comparison of heavy rainfall mechanisms in Korea and the central US. *J. Meteor. Soc. Japan*, **82**, 1469–1479, https://doi.org/10.2151/jmsj.2004.1469.

Horinouchi, T., 2014: Influence of upper tropospheric disturbances on the synoptic variability of precipitation and moisture transport over summertime East Asia and the northwestern Pacific. *J. Meteor. Soc. Japan*, **92**, 519–541, https://doi.org/10.2151/jmsj.2014-602.

——, and A. Hayashi, 2017: Meandering subtropical jet and precipitation over summertime East Asia and the northwestern Pacific. *J. Atmos. Sci.*, **74**, 1233–1247, https://doi.org/10.1175/JAS-D-16-0252.1.

Hoskins, B. J., and M. A. Pedder, 1980: The diagnosis of middle latitude synoptic development. *Quart. J. Roy. Meteor. Soc.*, **106**, 707–719, https://doi.org/10.1002/qj.49710645004.

Jo, E., C. Park, S.-W. Son, J.-W. Roh, G.-W. Lee, and Y.-H. Lee, 2020: Classification of localized heavy rainfall events in South Korea. *Asia-Pac. J. Atmos. Sci.*, **56**, 77–88, https://doi.org/10.1007/s13143-019-00128-7.

Johnson, N. C., 2013: How many ENSO flavors can we distinguish? *J. Climate*, **26**, 4816–4827, https://doi.org/10.1175/JCLI-D-12-00649.1.

Jung, I.-W., D.-H. Bae, and G. Kim, 2011: Recent trends of mean and extreme precipitation in Korea. *Int. J. Climatol.*, **31**, 359–370, https://doi.org/10.1002/joc.2068.

Jung, M.-I., S.-W. Son, H.-C. Kim, S.-W. Kim, and R. J. Park, 2019: Contrasting synoptic weather patterns between non-dust high particulate matter events and Asian dust events in Seoul, South Korea. *Atmos. Environ.*, **214**, 116864, https://doi.org/10.1016/j.atmosenv.2019.116864.

Kamae, Y., M. Wei, and S.-P. Xie, 2017: Climatological relationship between warm season atmospheric rivers and heavy rainfall over East Asia. *J. Meteor. Soc. Japan*, **95**, 411–431, https://doi.org/10.2151/jmsj.2017-027.

Kawasaki, K., Y. Tachibana, T. Nakamura, and K. Yamazaki, 2021: Role of the cold Okhotsk Sea on the climate of the North Pacific subtropical high and baiu precipitation. *J. Climate*, **34**, 495–507, https://doi.org/10.1175/JCLI-D-20-0432.1.

Keller, J. H., and Coauthors, 2019: The extratropical transition of tropical cyclones. Part II: Interaction with the midlatitude flow, downstream impacts, and implications in predictability. *Mon. Wea. Rev.*, **147**, 1077–1106, https://doi.org/10.1175/MWR-D-17-0329.1.

Keyser, D., M. J. Reeder, and R. J. Reed, 1988: A generalization of Petterssen's frontogenesis function and its relation to the forcing of vertical motion. *Mon. Wea. Rev.*, **116**, 762–781, https://doi.org/10.1175/1520-0493(1988)116<0762:AGOPFF>2.0.CO;2.

——, B. D. Schmidt, and D. G. Duffy, 1992: Quasigeostrophic vertical motions diagnosed from along- and cross-isentrope components of the Q vector. *Mon. Wea. Rev.*, **120**, 731–741, https://doi.org/10.1175/1520-0493(1992)120<0731:QVMDFA>2.0.CO;2.

Kim, G., and Coauthors, 2018: Future changes in extreme precipitation indices over Korea. *Int. J. Climatol.*, **38**, e862–e874, https://doi.org/10.1002/joc.5414.

Kodama, Y., 1992: Large-scale common features of subtropical precipitation zones (the Baiu frontal zone, the SPCZ, and the SACS) Part I: Characteristics of subtropical frontal zones. *J. Meteor. Soc. Japan*, **70**, 813–836, https://doi.org/10.2151/jmsj1965.70.4_813.

Kohonen, T., 1998: The self-organizing map. *Neurocomputing*, **21**, 1–6, https://doi.org/10.1016/S0925-2312(98)00030-7.

——, 2013: Essentials of the self-organizing map. *Neural Networks*, **37**, 52–65, https://doi.org/10.1016/j.neunet.2012.09.018.

Korea Meteorological Administration, 2011: *Typhoon White Book (in Korean)*. Korea Meteorological Administration, 342 pp., http://www.kma.go.kr/download_01/typhoon/typwhitebook_2011.pdf.

Lee, D.-K., J.-G. Park, and J.-W. Kim, 2008a: Heavy rainfall events lasting 19 days from July 31 to August 17, 1998, over Korea. *J. Meteor. Soc. Japan*, **86**, 313–333, https://doi.org/10.2151/jmsj.86.313.

——, J.-C. Ha, and J. Kim, 2008b: Application of the Sawyer-Eliassen equation to the interpretation of the synoptic-scale dynamics of a heavy rainfall case over East Asia. *Asia-Pac. J. Atmos. Sci.*, **44**, 49–68.

Lee, J.-Y., and Coauthors, 2017: The long-term variability of Changma in the East Asian summer monsoon system: A review and revisit. *Asia-Pac. J. Atmos. Sci.*, **53**, 257–272, https://doi.org/10.1007/s13143-017-0032-5.

Lee, S., 1999: The distribution of precipitation in Cheju Island (in Korean with English abstract). *J. Korean Geogr. Soc.*, **34**, 123–136.

Lee, T.-Y., and Y.-H. Kim, 2007: Heavy precipitation systems over the Korean Peninsula and their classification. *Asia-Pac. J. Atmos. Sci.*, **11**, 367–396.

Liu, W., L. Wang, D. Chen, K. Tu, C. Ruan, and Z. Hu, 2016: Large-scale circulation classification and its links to observed precipitation in the eastern and central Tibetan Plateau. *Climate Dyn.*, **46**, 3481–3497, https://doi.org/10.1007/s00382-015-2782-z.

Liu, Y., R. H. Weisberg, and C. N. K. Mooers, 2006: Performance evaluation of the self-organizing map for feature extraction. *J. Geophys. Res.*, **111**, C05018, https://doi.org/10.1029/2005JC003117.

Martin, J. E., 1999: Quasigeostrophic forcing of ascent in the occluded sector of cyclones and the trowal airstream. *Mon. Wea. Rev.*, **127**, 70–88, https://doi.org/10.1175/1520-0493(1999)127<0070:QFOAIT>2.0.CO;2.

——, 2006: The role of shearwise and transverse quasigeostrophic vertical motions in the midlatitude cyclone life cycle. *Mon. Wea. Rev.*, **134**, 1174–1193, https://doi.org/10.1175/MWR3114.1.

——, 2007: Lower-tropospheric height tendencies associated with the shearwise and transverse components of quasigeostrophic vertical motion. *Mon. Wea. Rev.*, **135**, 2803–2809, https://doi.org/10.1175/MWR3416.1.

Moore, B. J., D. Keyser, and L. F. Bosart, 2019: Linkages between extreme precipitation events in the central and eastern U.S.

and Rossby wave breaking. *Mon. Wea. Rev.*, **147**, 3327–3349, https://doi.org/10.1175/MWR-D-19-0047.1.

Moore, J. T., and G. E. Vanknowe, 1992: The effect of jet-streak curvature on kinematic fields. *Mon. Wea. Rev.*, **120**, 2429–2441, https://doi.org/10.1175/1520-0493(1992)120<2429:TEOJSC>2.0.CO;2.

Nguyen-Le, D., T. J. Yamada, and D. Tran-Anh, 2017: Classification and forecast of heavy rainfall in northern Kyushu during Baiu season using weather pattern recognition. *Atmos. Sci. Lett.*, **18**, 324–329, https://doi.org/10.1002/asl.759.

Nigro, M. A., and J. J. Cassano, 2014: Identification of surface wind patterns over the Ross Ice Shelf, Antarctica, using self-organizing map. *Mon. Wea. Rev.*, **142**, 2361–2378, https://doi.org/10.1175/MWR-D-13-00382.1.

Ninomiya, K., 1984: Characteristics of Baiu front as a predominant subtropical front in the summer Northern Hemisphere. *J. Meteor. Soc. Japan*, **62**, 880–894, https://doi.org/10.2151/jmsj1965.62.6_880.

Ohba, M., S. Kadokura, Y. Yoshida, D. Nohara, and Y. Toyoda, 2015: Anomalous weather patterns in relation to heavy precipitation events in Japan during the baiu season. *J. Hydrometeor.*, **16**, 688–701, https://doi.org/10.1175/JHM-D-14-0124.1.

Park, C., and Coauthors, 2021a: Record-breaking summer rainfall in South Korea in 2020: Synoptic characteristics and the role of large-scale circulations. *Mon. Wea. Rev.*, **149**, 3085–3100, https://doi.org/10.1175/MWR-D-21-0051.1.

——, S.-W. Son, and J.-H. Kim, 2021b: Role of baroclinic trough in triggering vertical motion during summertime heavy rainfall events in Korea. *J. Atmos. Sci.*, **78**, 1687–1702, https://doi.org/10.1175/JAS-D-20-0216.1.

——, ——, and H. Kim, 2021c: Distinct features of atmospheric rivers in the early versus late East Asian summer monsoon and their impacts on monsoon rainfall. *J. Geophys. Res. Atmos.*, **126**, e2020JD033537, https://doi.org/10.1029/2020JD033537.

Petterssen, S., 1936: *Contribution to the Theory of Frontogenesis*. Vol. 11, Cammermeyer, 27 pp.

Quinting, J. F., and S. C. Jones, 2016: On the impact of tropical cyclones on Rossby wave packets: A climatological perspective. *Mon. Wea. Rev.*, **144**, 2021–2048, https://doi.org/10.1175/MWR-D-14-00298.1.

Reusch, D. B., R. B. Aley, and B. C. Hewitson, 2005: Relative performance of self-organizing maps and principal component analysis in pattern extraction from synthetic climatological data. *Polar Geogr.*, **29**, 188–212, https://doi.org/10.1080/789610199.

Rousi, E., C. Anagnostopoulou, K. Tolika, and P. Maheras, 2015: Representing teleconnection patterns over Europe: A comparison of SOM and PCA methods. *Atmos. Res.*, **152**, 123–137, https://doi.org/10.1016/j.atmosres.2013.11.010.

Ryu, Y., and Coauthors, 2021: A multi-inventory ensemble analysis of the effects of atmospheric rivers on precipitation and streamflow in the Namgang-Dam Basin in Korea. *Water Resour. Res.*, **57**, e2021WR030058, https://doi.org/10.1029/2021WR030058.

Schumacher, R. S., and R. H. Johnson, 2008: Mesoscale processes contributing to extreme rainfall in a midlatitude warm-season flash flood. *Mon. Wea. Rev.*, **136**, 3964–3986, https://doi.org/10.1175/2008MWR2471.1.

Seo, K.-H., J.-H. Son, J.-Y. Lee, and H.-S. Park, 2015: Northern East Asian monsoon precipitation revealed by airmass variability and its prediction. *J. Climate*, **28**, 6221–6233, https://doi.org/10.1175/JCLI-D-14-00526.1.

Shin, U., T.-Y. Lee, and S.-H. Park, 2019: Environment and processes for heavy rainfall in the early morning over the Korean Peninsula during episodes of cloud clusters associated with mesoscale troughs. *J. Meteor. Soc. Japan*, **97**, 633–655, https://doi.org/10.2151/jmsj.2019-036.

Sohn, B. J., G.-H. Ryu, H.-J. Song, and M.-L. Oh, 2013: Characteristic features of warm-type rain producing heavy rainfall over the Korean Peninsula inferred from TRMM measurements. *Mon. Wea. Rev.*, **141**, 3873–3888, https://doi.org/10.1175/MWR-D-13-00075.1.

Sun, J., and T.-Y. Lee, 2002: A numerical study of an intense quasi-stationary convection band over the Korean Peninsula. *J. Meteor. Soc. Japan*, **80**, 1221–1245, https://doi.org/10.2151/jmsj.80.1221.

Tomita, T., T. Yamaura, and T. Hashimoto, 2011: Interannual variability of the Baiu season near Japan evaluated from the equivalent potential temperature. *J. Meteor. Soc. Japan*, **89**, 517–537, https://doi.org/10.2151/jmsj.2011-507.

Wang, B., and LinHo, 2002: Rainy season of the Asian–Pacific summer monsoon. *J. Climate*, **15**, 386–398, https://doi.org/10.1175/1520-0442(2002)015<0386:RSOTAP>2.0.CO;2.

——, R. Wu, and K. Lau, 2001: Interannual variability of the Asian summer monsoon: Contrasts between the Indian and the western North Pacific–East Asian monsoons. *J. Climate*, **14**, 4073–4090, https://doi.org/10.1175/1520-0442(2001)014<4073:IVOTAS>2.0.CO;2.

Yuan, Z. P., X. Y. Zhuge, and Y. Wang, 2020: The forced secondary circulation of the Mei-yu front. *Adv. Atmos. Sci.*, **37**, 766–780, https://doi.org/10.1007/s00376-020-9177-8.

Zhao, Y., and Coauthors, 2019: The large-scale circulation patterns responsible for extreme precipitation over the North China plain in midsummer. *J. Geophys. Res. Atmos.*, **124**, 12 794–12 809, https://doi.org/10.1029/2019JD030583.